



Mean flow and turbulence in unsteady canopy layers

Weiye Li¹ and Marco G. Giometto^{1,†}

¹Department of Civil Engineering and Engineering Mechanics, Columbia University, NY 10027, USA

(Received 24 August 2022; revised 7 September 2023; accepted 8 September 2023)

Non-stationarity is the rule in the atmospheric boundary layer (ABL). Under such conditions, the flow may experience departures from equilibrium with the underlying surface stress, misalignment of shear stresses and strain rates, and three-dimensionality in turbulence statistics. Existing ABL flow theories are primarily established for statistically stationary flow conditions and cannot predict such behaviours. Motivated by this knowledge gap, this study analyses the impact of time-varying pressure gradients on mean flow and turbulence over urban-like surfaces. A series of large-eddy simulations of pulsatile flow over cuboid arrays is performed, programmatically varying the oscillation amplitude α and forcing frequency ω . The analysis focuses on both longtime-averaged and phase-dependent flow dynamics. Inspection of longtime-averaged velocity profiles reveals that the aerodynamic roughness length z_0 increases with α and ω , whereas the displacement height d appears to be insensitive to these parameters. In terms of oscillatory flow statistics, it is found that α primarily controls the oscillation amplitude of the streamwise velocity and Reynolds stresses, but has a negligible impact on their wall-normal structure. On the other hand, ω determines the size of the region affected by the unsteady forcing, which identifies the so-called Stokes layer thickness δ_s . Within the Stokes layer, phase-averaged resolved Reynolds stress profiles feature substantial variations during the pulsatile cycle, and the turbulence is out of equilibrium with the mean flow. Two phenomenological models have been proposed that capture the influence of flow unsteadiness on z_0 and δ_s , respectively.

Key words: boundary layer structure, atmospheric flows, turbulent boundary layers

1. Introduction

Advancing our conceptual understanding and ability to predictively model exchange processes between urban areas and the atmosphere is of critical importance to a wide

† Email address for correspondence: mg3929@columbia.edu

range of applications, including urban air quality control (Britter & Hanna 2003; Barlow, Harman & Belcher 2004; Pascheke, Barlow & Robins 2008), urban microclimate studies (Roth 2012; Li & Bou-Zeid 2014; Ramamurthy, Li & Bou-Zeid 2017) and weather and climate forecasting (Holtslag *et al.* 2013), to name but a few. It hence comes as no surprise that substantial efforts have been devoted towards this goal over the past decades, via, e.g. numerical simulations (Bou-Zeid, Meneveau & Parlange 2004; Xie, Coceal & Castro 2008; Cheng & Porté-Agel 2015; Giometto *et al.* 2016; Auvinen *et al.* 2017; Sadique *et al.* 2017; Zhu *et al.* 2017; Li & Bou-Zeid 2019), wind tunnel experiments (Raupach, Thom & Edwards 1980; Böhm *et al.* 2013; Marucci & Carpentieri 2020) and observational studies (Rotach 1993; Kastner-Klein & Rotach 2004; Rotach *et al.* 2005; Christen, Rotach & Vogt 2009). These studies have explored the functional dependence of flow statistics on urban canopy geometry (Lettau 1969; Raupach 1992; Macdonald, Griffiths & Hall 1998; Coceal & Belcher 2004; Yang *et al.* 2016; Li & Katul 2022), characterized the topology of coherent structures (Kanda, Moriwaki & Kasamatsu 2004; Christen, van Gorsel & Vogt 2007; Coceal *et al.* 2007; Li & Bou-Zeid 2011; Inagaki *et al.* 2012) and derived scaling laws for scalar transfer between the urban canopy and the atmosphere (Pascheke *et al.* 2008; Cheng & Porté-Agel 2016; Li & Bou-Zeid 2019), amongst others. Most of the previous works have focused on atmospheric boundary layer (ABL) flow under (quasi) stationary conditions. However, stationarity is a rare occurrence in the ABL (Mahrt & Bou-Zeid 2020), and theories based on equilibrium turbulence are, therefore, often unable to grasp the full range of physics characterizing ABL flow environments.

Major drivers of non-stationarity in the ABL include time-varying horizontal pressure gradients, associated with non-turbulent motions ranging from submeso to synoptic scales, and time-dependent thermal forcings, induced by the diurnal cycle or by cloud-induced time variations of the incoming solar radiation (Mahrt & Bou-Zeid 2020). These conditions often result in departures from equilibrium turbulence, with important implications on time- and area-averaged exchange processes between the land surface and the atmosphere. The first kind of non-stationarity was examined in Mahrt (2007, 2008) and Mahrt *et al.* (2013), which showed that time-variations of the driving pressure gradient could enhance momentum transport under strong stable atmospheric stratifications. The second kind of non-stationarity was instead analysed in Hicks *et al.* (2018), making use of data from different field campaigns, and showed that the surface heat flux could change so rapidly during the morning and late afternoon transition that the relations for equilibrium turbulence no longer hold.

Numerical studies have also been recently conducted to study how exchange processes between the land surface and the atmosphere are modulated by non-stationarity in the ABL. In their study, Edwards, Edwards, Beare & Lapworth (2006) conducted a comparison of a prevailing single-column model based on equilibrium turbulence theories with the observations of an evening transition ABL, as well as results from large-eddy simulations (LES). Their findings emphasized the inadequacy of equilibrium turbulence theories in capturing the complex behaviour of ABL flows during rapid changes in thermal surface forcing. This breakdown of equilibrium turbulence was particularly notable during the evening transition period, which is known for its rapid changes in thermal forcing. Momen & Bou-Zeid (2017) investigated the response of the Ekman boundary layer to oscillating pressure gradients, and found that quasiequilibrium turbulence is maintained only when the oscillation period is much larger than the characteristic time scale of the turbulence. The majority of the efforts have focused on ABL flow over modelled roughness, where the flow dynamics in the roughness sublayer – that layer of the atmosphere that extends from the ground surface up to approximately 2–5 times the

mean height of roughness elements (Fernando 2010) – are bypassed, and surface drag is usually evaluated via an equilibrium wall-layer model (see, e.g. Momen & Bou-Zeid 2017), irrespective of the equilibrium-theory limitations outlined above. It hence remains unclear how unsteadiness impacts flow statistics and the structure of atmospheric turbulence in the roughness sublayer. Roughness sublayer flow directly controls exchanges of mass, energy and momentum between the land surface and the atmosphere, and understanding the dependence of flow statistics and structural changes in the turbulence topology on flow unsteadiness is therefore important in order to advance our ability to understand and predictively model these flow processes.

This study contributes to addressing this knowledge gap by focusing on non-stationarity roughness sublayer flow induced by time-varying pressure gradients. Unsteady pressure gradients in the real-world ABL can be characterized by periodic and aperiodic variations in both magnitude and direction. In this study, we limit our attention to a pulsatile streamwise pressure-gradient forcing, consisting of a constant mean and a sinusoidal oscillating component. This approach has two major merits. First, the temporal evolution of flow dynamics and associated statistics, as well as structural changes in turbulence, can be easily characterized thanks to the time-periodic nature of the flow unsteadiness. Second, the time scale of the pulsatile forcing is well defined, and can hence be varied programmatically to encompass a range of representative flow regimes.

Pulsatile turbulent flows over aerodynamically smooth surfaces have been the subject of active research in the mechanical engineering community because of their relevance across a range of applications; these include industrial (e.g. a rotating or poppet valve) and biological (blood in arteries) flows. The corresponding laminar solution is an extension of Stokes’s second problem (Stokes 1901), where the modulation of the flow field by an unsteady pressure gradient is confined to a layer of finite thickness known as the ‘Stokes layer’. The thickness of the Stokes layer δ_s is a function of the pulsatile forcing frequency ω , i.e. $\delta_s = 2l_s$, where $l_s = \sqrt{2\nu/\omega}$ is the so-called Stokes length scale and ν is the kinematic viscosity of the fluid. In the turbulent flow regime, it has been found that the characteristics of the pulsatile flow are not only dependent on the forcing frequency, but also on the amplitude of the oscillation. Substantial efforts have been devoted to investigating this problem, from both an experimental (Ramaprian & Tu 1980, 1983; Tu & Ramaprian 1983; Mao & Hanratty 1986; Brereton, Reynolds & Jayaraman 1990; Tardu & Binder 1993; Tardu 2005) and a computational perspective (Scotti & Piomelli 2001; Manna, Vacca & Verzicco 2012, 2015; Weng, Boij & Hanifi 2016). Scotti & Piomelli (2001) drew an analogy to the Stokes length and proposed a turbulent Stokes length scale, which can be expressed in inner units as

$$l_t^+ = \frac{u_\tau}{\nu} \left(\frac{2(\nu + \nu_t)}{\omega} \right)^{1/2}, \quad (1.1)$$

where u_τ is the friction velocity based on the surface friction averaged over pulsatile cycles and ν_t is the so-called eddy viscosity. Parameterizing the eddy viscosity in terms of the Stokes turbulent length scale, i.e. $\nu_t = \kappa u_\tau l_t$, where κ is the von Kármán constant, and substituting into (1.1) one obtains

$$l_t^+ = l_s^+ \left(\frac{\kappa l_s^+}{2} + \left(1 + \left(\frac{\kappa l_s^+}{2} \right)^{1/2} \right) \right). \quad (1.2)$$

When l_t^+ is large (e.g. when $\omega \rightarrow 0$), the flow is in a quasisteady state. Under such a condition, the flow at each pulsatile phase resembles a statistically stationary boundary

layer flow, provided that the instantaneous friction velocity is used to normalize statistics. As ω increases and l_t^+ becomes of the order of the open channel height L_3^+ , the entire flow is affected by the pulsation, i.e. time lags occur between flow statistics at different elevations, and turbulence undergoes substantial structural changes from its equilibrium configuration. When $l_t^+ < L_3^+/2$, the flow modulation induced by the pulsation is confined within the Stokes layer $\delta_s^+ = 2l_t^+$. Above the Stokes layer, one can observe a plug-flow region, with the turbulence being frozen to its equilibrium configuration and simply advected by the mean flow pulsation. A few years later, Bhaganagar (2008) conducted a series of direct numerical simulations (DNS) of low-Reynolds-number pulsatile flow over transitionally rough surfaces. She found that flow responses to pulsatile forcing are generally similar to those in smooth-wall cases, when the roughness size is of the same order of magnitude as the viscous sublayer thickness. The only exception is that, as the pulsation frequency approaches the frequency of vortex shedding from the roughness elements, the longtime averaged velocity profile deviates significantly from that of the steady flow case due to the resonance between the pulsation and the vortex shedding. In the context of a similar flow system, Patil & Fringer (2022) also reported a comparable observation in their DNS study.

In addition to the work of Bhaganagar (2008) and Patil & Fringer (2022), pulsatile flow over small-scale roughness, e.g. sand grain roughness, has also been studied extensively in the oceanic context, i.e. combined current-wave boundary layers, which play a crucial role in controlling sediment transport and associated erosion in coastal environments (Grant & Madsen 1979; Kemp & Simons 1982; Myrhaug & Slaattelid 1989; Sleath 1991; Soulsby *et al.* 1993; Mathisen & Madsen 1996; Fredsøe, Andersen & Sumer 1999; Yang *et al.* 2006; Yuan & Madsen 2015). The thickness of the wave boundary layer, which is the equivalent of the Stokes layer in the engineering community, is defined as

$$\delta_w = \frac{2ku_{\tau,max}}{\omega}, \quad (1.3)$$

where $u_{\tau,max} = \sqrt{\tau_{max}}$, and τ_{max} denotes the maximum of kinematic shear stress at the surface during the pulsatile cycle. Within the wave boundary layer, mean flow and turbulence are controlled by the nonlinear interaction between currents and waves. Above this region, the modulation of turbulence by waves vanishes. The wall-normal distribution of the averaged velocity over the pulsatile cycle deviates from the classic logarithmic profile, and is characterized by a ‘two-log’ profile, i.e. the velocity exhibits a logarithmic profile with the actual roughness length within the wave boundary layer and a different one characterized by a larger roughness length further aloft (Grant & Madsen 1986; Fredsøe *et al.* 1999; Yang *et al.* 2006; Yuan & Madsen 2015). Such behaviour was first predicted by a two-layer time-invariant eddy viscosity model by Grant & Madsen (1979), followed by many variants and improvements (Myrhaug & Slaattelid 1989; Sleath 1991; Yuan & Madsen 2015).

On the contrary, pulsatile flow at high Reynolds numbers over large roughness elements, such as buildings, has received far less attention. Yu, Rosman & Hench (2022) conducted a series of LES of combined wave-current flows over arrays of hemispheres, which can be seen as a surrogate of reefs near the coastal ocean. They focused only on low Keulegan–Carpenter numbers $KC \sim O(1-10)$, where KC is defined as the ratio between the wave excursion $U_w T$ and the diameter of the hemispheres, and U_w and T are the wave orbital velocity and the wave period, respectively (Keulegan *et al.* 1958). However, conclusions from Yu *et al.* (2022) cannot be readily applied to pulsatile flow over urban-like roughness (i.e. large obstacles with sharp edges), mainly

because different surface morphologies yield distinct air–canopy interaction regimes under pulsatile forcings (Carr & Plesniak 2017).

Motivated by this knowledge gap, this study proposes a detailed analysis on the dynamics of the mean flow and turbulence in high-Reynolds-number pulsatile flow over idealized urban canopies. The analysis is carried out based on a series of LES of pulsatile flow past an array of surface-mounted cuboids, where the frequency and amplitude of the pressure gradient are programmatically varied. The LES technique has been shown to be capable of capturing the major flow features of pulsatile flow over various surface conditions (Scotti & Piomelli 2001; Chang & Scotti 2004). The objective of this study is to answer fundamental questions pertaining to the impacts of the considered flow unsteadiness on the mean flow and turbulence in the urban boundary layer:

- (i) Does the presence of flow unsteadiness alter the mean flow profile in a longtime-averaged sense? If so, how do such modifications reflect in the aerodynamic surface parameters?
- (ii) To what extent does the unsteady pressure gradient impact the overall momentum transport and turbulence generation in a longtime-averaged sense within and above the canopy?
- (iii) How do the phase-averaged mean flow and turbulence behave in response to the periodically varying pressure gradient? How are such phase-dependent behaviours controlled by the oscillation amplitude and the forcing frequency?

This paper is organized as follows. Section 2 introduces the numerical algorithm and the set-up of simulations, along with the flow decomposition and averaging procedure. Results are presented and discussed in § 3. Concluding remarks are given in § 4.

2. Methodology

2.1. Numerical procedure

A suite of LES is performed using an extensively validated in-house code (Albertson & Parlange 1999*a,b*; Bou-Zeid, Meneveau & Parlange 2005; Chamecki, Meneveau & Parlange 2009; Anderson, Li & Bou-Zeid 2015; Fang & Porté-Agel 2015; Giometto *et al.* 2016; Li *et al.* 2016). The code solves the filtered continuity and momentum transport equations in a Cartesian reference system, which read

$$\frac{\partial u_i}{\partial x_i} = 0, \quad (2.1)$$

$$\frac{\partial u_i}{\partial t} + u_j \left(\frac{\partial u_i}{\partial x_j} - \frac{\partial u_j}{\partial x_i} \right) = -\frac{1}{\rho} \frac{\partial p^*}{\partial x_i} - \frac{\partial \tau_{ij}}{\partial x_j} - \frac{1}{\rho} \frac{\partial p_\infty}{\partial x_1} \delta_{i1} + F_i, \quad (2.2)$$

where u_1 , u_2 and u_3 are the filtered velocities along the streamwise (x_1), cross-stream (x_2) and wall-normal (x_3) direction, respectively. The advection term is written in the rotational form to ensure kinetic energy conservation in the discrete sense (Orszag & Pao 1975). Here ρ represents the constant fluid density, τ_{ij} is the deviatoric component of the subgrid-scale (SGS) stress tensor, which is evaluated via the scale-dependent dynamic (LASD) Smagorinsky model (Bou-Zeid *et al.* 2005). The LASD model has been extensively validated in wall-modelled simulations of unsteady ABL flow (Momen & Bou-Zeid 2017; Salesky, Chamecki & Bou-Zeid 2017) and in the simulation of flow over surface-resolved urban-like canopies (Anderson *et al.* 2015; Giometto *et al.* 2016; Li *et al.* 2016; Yang 2016). Note that viscous stresses are neglected in the current study; this

assumption is valid as the typical Reynolds number of the ABL flows is $Re \sim O(10^9)$, and the flow is in the fully rough regime. Here $p^* = p + \frac{1}{3}\rho\tau_{ii} + \frac{1}{2}\rho u_i u_i$ is the modified pressure, which accounts for the trace of SGS stress and resolved turbulent kinetic energy. The flow is driven by a spatially uniform but temporally periodic pressure gradient, i.e.

$$-\partial p_\infty / \partial x_1 = \rho f_m [1 + \alpha_p \sin(\omega t)], \quad (2.3)$$

where f_m denotes the mean pressure gradient. Here α_p is a constant controlling the amplitude of the forcing, ω represents the forcing frequency and δ_{ij} is the Kronecker delta tensor.

Periodic boundary conditions apply in the wall-parallel directions, and free-slip boundary conditions are employed at the upper boundary. The lower surface is representative of an array of uniformly distributed cuboids, which serves as a surrogate of urban landscapes. This approach has been commonly adopted in fundamental studies of ABL processes due to its limited number of characteristic length scales, which makes it amenable to comprehensive examination and analytical treatment (Reynolds & Castro 2008; Cheng & Porté-Agel 2015; Tomas, Pourquie & Jonker 2016; Basley, Perret & Mathis 2019; Omidvar *et al.* 2020). Such an approach is justified on the basis that one should first study a problem in its simplest set-up before introducing additional complexities. Nonetheless, it is important to acknowledge that the introduction of randomness in roughness alters the flow characteristics and the generation of turbulence in rough-wall boundary layer flows. For example, Xie *et al.* (2008) studied flows over random urban-like obstacles and found that turbulence features in the roughness sublayer are controlled by the randomness in the roughness. Giometto *et al.* (2016) conducted an LES study and highlighted that roughness randomness enhances the dispersive stress in the roughness sublayer. Chau & Bhaganagar (2012) carried out a series of DNS of flow over transitionally rough surfaces, demonstrating that different levels of roughness randomness lead to distinct turbulence structures in the near-wall region and subsequently affect turbulence intensities.

Spatial derivatives in the wall-parallel directions are computed via a pseudospectral collocation method based on truncated Fourier expansions (Orszag 1970), whereas a second-order staggered finite difference scheme is employed in the wall-normal direction. A second-order Adams–Bashforth scheme is adopted for time integration. Nonlinear advection terms are dealiased via the 3/2 rule (Canuto *et al.* 2007; Margairaz *et al.* 2018). Roughness elements are explicitly resolved via a discrete-forcing immersed boundary method (IBM) (Mittal & Iaccarino 2005), which is also commonly referred to as the direct forcing IBM (Mohd-Yusof 1996; Fang *et al.* 2011). The IBM was originally developed in Mohd-Yusof (1996) and first introduced to ABL studies by Chester, Meneveau & Parlange (2007). Since then, the IBM has been extensively validated in subsequent studies (e.g. Graham & Meneveau 2012; Cheng & Porté-Agel 2015; Anderson 2016; Giometto *et al.* 2016; Yang & Anderson 2018; Li & Bou-Zeid 2019). Specifically, an artificial force F_i drives the velocity to zero within the cuboids, and an inviscid equilibrium logarithmic wall-layer model (Moeng 1984; Giometto *et al.* 2016) is applied over a narrow band centred at the fluid–solid interface to evaluate the wall stresses. As shown in Appendix A, for flow over cuboids in the fully rough regime, the use of an equilibrium wall model does not impact the flow field significantly. Xie & Castro (2006) reached a similar conclusion for a comparable flow system. The incompressibility condition is then enforced via a pressure-projection approach Kim & Moin (1985).

Figure 1 shows a schematic of the computational domain. The size of the domain is $[0, L_1] \times [0, L_2] \times [0, L_3]$ with $L_1 = 72h$, $L_2 = 24h$ and $L_3 = 8h$, where h is the height of

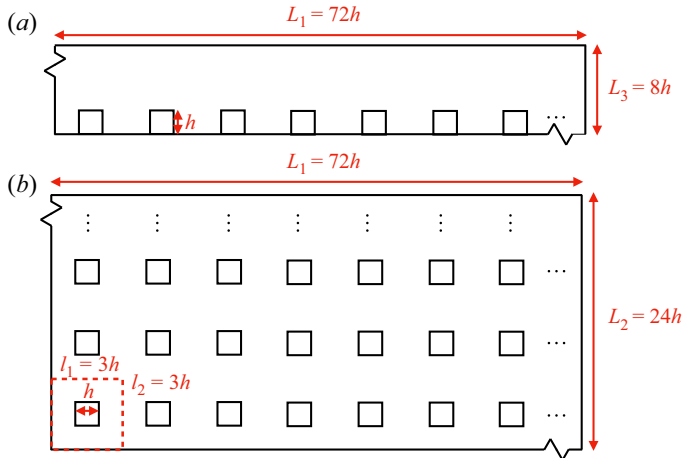


Figure 1. Side and planar view of the computational domain (*a,b*, respectively). The red dashed line denotes the repeating unit.

the cuboids. The planar and frontal areas of the cube array are set to $\lambda_p = \lambda_f = 0.1$. As such, the lower surface is comprised of $(n_1, n_2) = (24, 8)$ repeating units with dimensions of $(l_1, l_2) = (3h, 3h)$. An aerodynamic roughness length of $z_0 = 10^{-4}h$ is prescribed at the cube surfaces and the lower surface via the wall-layer model. With the chosen value of z_0 , the SGS pressure drag is a negligible contributor to the overall momentum balance (Yang & Meneveau 2016). The domain is discretized using a uniform Cartesian grid $(N_1, N_2, N_3) = (576, 192, 128)$ where each cube is resolved by $(8, 8, 16)$ grid points. As shown in Appendix B, this resolution yields flow statistics – up to second-order moments – that are poorly sensitive to grid resolution.

2.2. Averaging operations

Given the inherent time-periodicity of the flow system, phase averaging is the natural approach to evaluate flow statistics in pulsatile flows (Scotti & Piomelli 2001; Bhaganagar 2008; Weng *et al.* 2016; Önder & Yuan 2019). Throughout the paper, $\overline{(\cdot)}$ denotes the phase averaging operation. Specifically, the phase average of a quantity of interest θ is defined as

$$\bar{\theta}(x_1, x_2, x_3, t) = \frac{1}{N_p n_1 n_2} \sum_{n=0}^{N_p-1} \sum_{i=0}^{n_1-1} \sum_{j=0}^{n_2-1} \theta(x_1 + il_1, x_2 + jl_2, x_3, t + nT),$$

$$0 \leq x_1 \leq l_1, \quad 0 \leq x_2 \leq l_2, \quad 0 \leq t \leq T, \quad (2.4)$$

where N_p denotes the number of the pulsatile cycles over which the averaging operation is performed, and $T = 2\pi/\omega$ is the time period of the pulsatile forcing.

In addition to phase averaging, we introduce an intrinsic spatial averaging operation (Schmid *et al.* 2019). This operation is conducted over a thin wall-parallel slab of fluid characterized by a thickness δ_3 , namely

$$\langle \bar{\theta} \rangle(x_3, t) = \frac{1}{V_f} \int_{x_3-\delta_3/2}^{x_3+\delta_3/2} \int_0^{l_2} \int_0^{l_1} \bar{\theta}(x_1, x_2, x_3, t) dx_1 dx_2 dx_3. \quad (2.5)$$

A given instantaneous quantity θ can be then decomposed as

$$\theta(x_1, x_2, x_3, t) = \langle \bar{\theta} \rangle(x_3, t) + \theta'(x_1, x_2, x_3, t), \quad (2.6)$$

where $(\cdot)'$ denotes a departure of the instantaneous value from the corresponding phase- and intrinsic-averaged quantity. A phase- and intrinsic-averaged quantity can be further decomposed into a longtime average and an oscillatory component with zero mean, i.e.

$$\langle \bar{\theta} \rangle(x_3, t) = \langle \bar{\theta} \rangle_l(x_3) + \langle \bar{\theta} \rangle_o(x_3, t). \quad (2.7)$$

This work relies on the Scotti & Piomelli (2001) approach to analyse the flow system; in this approach, an oscillatory quantity $\langle \bar{\theta} \rangle_o$ is split into two components: one corresponding to the flow oscillation at the forcing frequency (fundamental mode), and one which includes contributions from all of the remaining harmonics, i.e.

$$\langle \bar{\theta} \rangle_o(x_3, t) = A_\theta(x_3) \sin[\omega t + \phi_\theta(x_3)] + e_\theta(x_3), \quad (2.8)$$

where A_θ and ϕ_θ are the oscillatory amplitude of the fundamental mode and the phase lag with respect to the pulsatile forcing, respectively. These components are evaluated via minimization of $\|e_\theta\|_2$ at each x_3 .

2.3. Dimensional analysis and suite of simulations

Having fixed the domain size, the aerodynamic surface roughness length and the spatial discretization, the remaining physical parameters governing the problem are: (i) the oscillation amplitude α , defined as the ratio between the oscillation amplitude of $\langle \bar{u}_1 \rangle$ at the top of the domain and the corresponding mean value; (ii) the forcing frequency ω ; (iii) the friction velocity based on the mean pressure gradient $u_\tau = \sqrt{f_m L_3}$; and (iv) the height of roughness elements h . The latter is a characteristic length scale of the flow in the urban canopy layer (UCL), which is here defined as extending from the surface up to h . System response is studied in time and along the x_3 coordinate direction, so (v) the wall-normal elevation x_3 and (vi) time t should also be included in the parameter set. Note that the viscosity is not taken into account since the flow is in the fully rough regime. Choosing u_τ and h as repeating parameters, a given normalized longtime ($\langle \bar{Y} \rangle_l$) and oscillatory ($\langle \bar{Y} \rangle_o$) quantity of interest can hence be written as

$$\langle \bar{Y} \rangle_l = f\left(\frac{x_3}{h}, \frac{\omega h}{u_\tau}, \alpha\right), \quad \text{and} \quad \langle \bar{Y} \rangle_o = g\left(\frac{x_3}{h}, \frac{u_\tau}{h}t, \frac{\omega h}{u_\tau}, \alpha\right), \quad (2.9a,b)$$

respectively, where f and g are universal functions. Equation (2.9a,b) show that $\langle \bar{Y} \rangle_l$ and $\langle \bar{Y} \rangle_o$ only depend on two dimensionless parameters, namely α and ωT_h . Here $T_h = h/u_\tau$ is the turnover time of the largest eddies in the UCL and can be best understood as a characteristic time scale of the flow in the UCL. Here $\omega T_h \sim T_h/T$ is hence essentially the ratio between the turnover time of the largest eddies in the UCL (T_h) and the pulsation time period (T). Also note the normalized ω can be seen as an equivalent Strouhal number, which has been used as a non-dimensional parameter in earlier works for the considered flow system (see e.g. Tardu, Binder & Blackwelder 1994). Four different values of ωT_h are considered in this study, namely $\omega T_h = \{0.05\pi, 0.125\pi, 0.25\pi, 1.25\pi\}$. For $u_\tau \approx 0.1 \text{ m s}^{-1}$ and $h \approx 10 \text{ m}$ – common ABL values for these quantities (Stull 1988) – the considered ωT_h set encompasses time scales variability from a few seconds to several hours, which are representative of submesoscale ABL flow phenomena (Mahrt 2009; Hoover *et al.* 2015).

Acronym	Target α	Actual α	α_p	ωT_h
LL	0.2	0.17	2.4	0.05π
LM	0.2	0.16	6.0	0.125π
LH	0.2	0.16	12.0	0.25π
LVH	0.2	0.16	60.0	1.25π
HL	0.4	0.38	4.8	0.05π
HM	0.4	0.36	12.0	0.125π
HH	0.4	0.36	24.0	0.25π
HVH	0.4	0.37	120.0	1.25π
SS	0.0	0.0	0.0	—

Table 1. List of LES runs. The naming convention for pulsatile flow cases is as follows. The first letter represents the oscillation amplitude: L for $\alpha = 0.2$ and H for $\alpha = 0.4$. The second and third letters denote the forcing frequencies: L for $\omega T_h = 0.05\pi$, M for $\omega T_h = 0.125\pi$, H for $\omega T_h = 0.25\pi$ and VH for $\omega T_h = 1.25\pi$. Here SS denotes the statistically stationary flow case.

In this study, we aim to narrow our focus to the current-dominated regime, i.e. $0 < \alpha < 1$. Larger values of α would lead to a wave-dominated regime, which behaves differently. The set $\alpha = \{0.2, 0.4\}$ is here considered, which yields a non-trivial flow response while remaining sufficiently far from the wave-dominated regime. Due to the lack of a straightforward relation between the oscillatory pressure gradient (α_p) and α , α_p has been tuned iteratively to achieve the desired α . As shown in [table 1](#), despite the optimization process, there are still discernible discrepancies between the target α and its actual value. As also shown in previous works ([Scotti & Piomelli 2001](#); [Bhaganagar 2008](#)), α is highly sensitive to variations in α_p , which makes it challenging to prescribe its exact value via the imposed pressure gradient.

The suite of simulations and corresponding acronyms used in this study are listed in [table 1](#). A statistically stationary flow case ($\alpha = 0$) is also carried out to highlight departures of pulsatile flow cases from the steady state condition. Simulations with pulsatile forcing are initialized with velocity fields from the stationary flow case; the $\omega T_h = \{0.25\pi, 1.25\pi\}$ and $\omega T_h = \{0.05\pi, 0.125\pi\}$ cases are then integrated in time over $200T_{L_3}$ and $400T_{L_3}$, respectively, where $T_{L_3} = L_3/u_\tau$ is the turnover time of the largest eddies in the domain. This approach yields converged phase-averaged flow statistics. The size of the time step δt is chosen to satisfy the Courant–Friedrichs–Lewy stability condition $(u\delta t)/\delta_x \leq 0.05$, where u is the maximum velocity magnitude at any given spatial location and time during a run, and δ_x is the grid stencil in the computational domain. Instantaneous three-dimensional snapshots of the velocity and pressure fields are collected every $T/16$ for the $\omega T_h = \{0.25\pi, 1.25\pi\}$ cases and every $T/80$ for the $\omega T_h = \{0.05\pi, 0.125\pi\}$ cases, after an initial $20T_{L_3}$ transient period.

3. Results and discussion

3.1. Three-dimensional flow fields

To gain insights into the instantaneous flow field, [figure 2](#) displays the streamwise fluctuating velocity within and above the UCL from the HM case at two different x_3 planes and phases. The chosen phases, $t = 0$ and $t = T/2$, correspond to the end of the deceleration ($T/2 < t < T$) and acceleration ($0 < t < T/2$) periods, respectively.

It is apparent from [figure 2\(a,b\)](#) that meandering low-momentum ($u'_1 < 0$) streaks are flanked by adjacent high-momentum ($u'_1 > 0$) ones. Comparing these two, turbulence

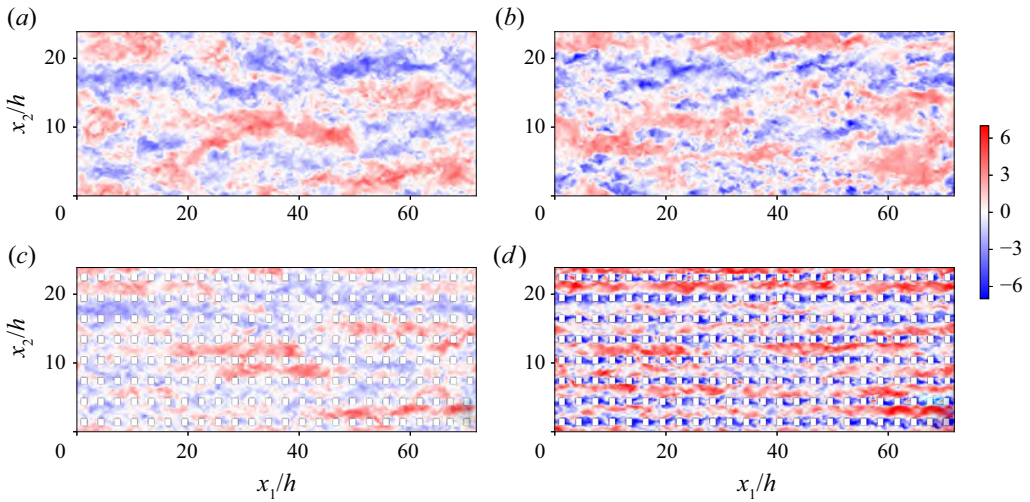


Figure 2. Normalized instantaneous streamwise fluctuating velocity field u'_1/u_τ at streamwise/cross-stream plane $x_3 = 2h$ (a,b) and $x_3 = 0.75h$ (c,d) from the HM case. Here $u_\tau = \sqrt{f_m L_3}$ is the friction velocity based on the mean pressure gradient. Panels (a,c) correspond to $t = 0$, whereas panels (b,d) correspond to $t = T/2$.

structures at $t = T/2$ appear smaller in size in both streamwise and spanwise directions. Additionally, within the UCL, apparent vortex shedding occurs on the lee side of the cubes at $t = T/2$, while it is less pronounced at $t = 0$. This suggests that flow unsteadiness substantially modifies the flow field during the pulsatile cycle and is expected to impact the flow statistics.

For a more comprehensive understanding of the phase-averaged flow pattern, figure 3 displays vector plots of (\bar{u}_1, \bar{u}_2) at $x_3/h = 0.75$ for the LL and HVH cases. These cases feature the weakest and strongest departures from the statistically stationary flow regime, and the authors have verified that they comprehensively capture the range of flow variability within the considered suite of simulations. Colours in the figure depict the signed wall-parallel swirl strength λ , providing a visualization of the phase-averaged vortex morphology. The definition of λ is in line with the approach of Stanislas, Perret & Foucaut (2008) and Elsinga *et al.* (2012). The magnitude of λ is the absolute value of the imaginary part of the eigenvalue of the reduced velocity gradient tensor \mathbf{J}_{12} , which is

$$\mathbf{J}_{12} = \begin{pmatrix} \partial \bar{u}_1 / \partial x_1 & \partial \bar{u}_1 / \partial x_2 \\ \partial \bar{u}_2 / \partial x_1 & \partial \bar{u}_2 / \partial x_2 \end{pmatrix}. \quad (3.1)$$

The sign of λ is determined by the vorticity component ω_3 and differentiates regions of anticlockwise (positive) and clockwise (negative) swirling motions.

As shown in figure 3(a), the LL case exhibits a consistent vortex distribution throughout the pulsatile cycle. Strong shear layers manifest at the leading edges of the cuboid element, and the wake region is characterized by a pair of counter-rotating vortices. Such a vortex pair corresponds to an arch- or horseshoe-type vortex arising from the merging of recirculation vortices, which originate at the trailing edges of the top and sidewalls of the roughness element. It has been frequently observed in the wake of obstacles with height-width aspect ratios near unity. For further details, the reader is referred to Martinuzzi & Tropea (1993), Pattenden, Turnock & Zhang (2005) and Gonçalves *et al.* (2015). In marked contrast, flow unsteadiness considerably modifies the flow pattern in the HVH case. Specifically, during the flow deceleration, the shear layers at the leading edges

Mean flow and turbulence in unsteady canopy layers

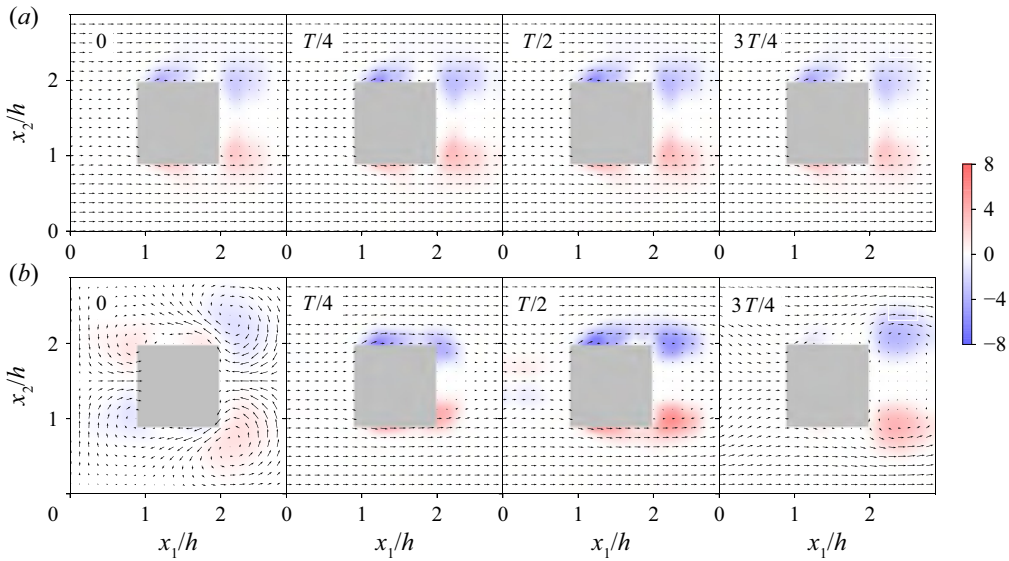


Figure 3. Vector plots of the phase-averaged velocity at the $x_3/h = 0.75$ wall-parallel plane from LL (a) and HVH (b) cases. Colour contours represent the wall-normal swirling strength λ .

vanish due to flow reversal, i.e. $\bar{u}_1 < 0$. During flow deceleration, the strength of the vortex pair is attenuated as its cores separate and distance themselves from the cuboid element, and the process is reversed during the acceleration. This behaviour is in line with findings from wind tunnel experiments of pulsatile flow over an isolated cube by Carr & Plesniak (2017).

Further insight can be obtained by considering variations in the normalized phase-averaged streamwise velocity, which are shown in figure 4 over a vertical transect for the LL and HVH cases. Acceleration and deceleration periods are apparent from the variations of the colour intensity in the above-UCL region, with the largest phase-averaged velocity magnitudes characterizing the end of the acceleration period, and lower ones the end of the deceleration. Dashed lines in figure 4 highlight that the flow is rather homogeneous above the UCL throughout the cases and that flow pulsation has a weak impact on the thickness of the roughness sublayer. Within the UCL, the LL case features modest variations in the structure of the phase-averaged streamwise velocity field; such a quantity retains approximately the same spatial structure throughout the pulsatile cycle and only varies in magnitude, with larger magnitudes occurring at $t = T/2$. Phase variations in the phase-averaged streamwise velocity become again more apparent and interesting as the forcing frequency and amplitude increase, with the HVH case featuring ample regions of negative phase-averaged velocity at $t = 0$ (end of flow deceleration) and $t = 3T/4$ (decelerating flow), and nearly lack thereof at $T/4$ (accelerating flow). Further, the largest negative phase-averaged velocity within the UCL occurs at $t = 3T/4$ rather than at $T/2$ as for the LL case, highlighting the presence of a different coupling between the UCL and the flow aloft. Note that all of the considered cases feature a relatively strong shear layer separating from the trailing edge of the cube, leading to enhanced local production of turbulent kinetic energy and transition from surface layer (above h) to canopy layer dynamics within the UCL. These observations, while still qualitative in nature, provide a first glimpse on complexities associated with the considered flow system and how it

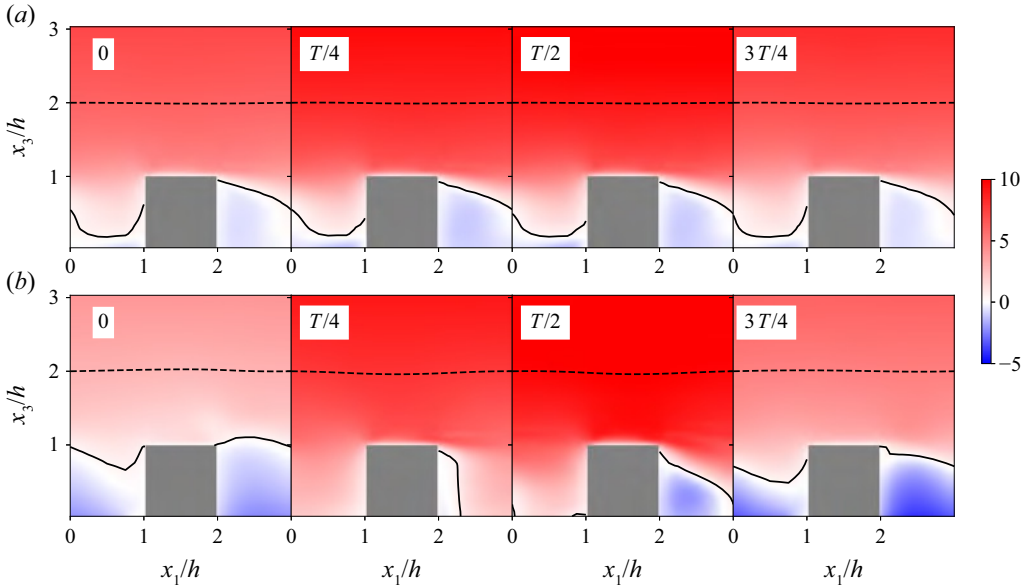


Figure 4. Phase-averaged streamwise velocity \bar{u}_1/u_τ at the streamwise/vertical plane through the centre of the cube, i.e. $x_2 = 1.5h$, for low-amplitude cases: LL (a) and HVH (b). The fields depicted in different panels are $T/4$ apart. Solid contour lines denote $\bar{u}_1/u_\tau = 0$. Dashed contour lines represent $\bar{u}_1 = \bar{u}_1(0, 1.5h, 2h)$.

responds to a range of forcing amplitudes and frequencies. The next sections will delve into a more detailed quantitative analysis.

3.2. Longtime-averaged statistics

3.2.1. Longtime-averaged velocity profile

Profiles of the longtime-averaged streamwise velocity are shown in figure 5. Flow unsteadiness leads to a horizontal shift of profiles in the proposed semilogarithmic plot. This behaviour is distinct from the ‘two-log’ profile in flow over sand grain roughness (Fredsoe *et al.* 1999; Yang *et al.* 2006; Yuan & Madsen 2015), and also in stark contrast to the one previously observed in current-dominated pulsatile flow over aerodynamically smooth surfaces, where the longtime-averaged field is essentially unaffected by flow unsteadiness (Tardu & Binder 1993; Scotti & Piomelli 2001; Tardu 2005; Manna *et al.* 2012; Weng *et al.* 2016). As also apparent from figure 5, departures from the statistically stationary flow profile become more significant for larger values of α and ω .

Variations in the aerodynamic roughness length z_0 and displacement height d parameters with ωT_h are shown in figure 6 for the considered canopy. These parameters are evaluated via the Macdonald *et al.* (1998) approach, where d is the barycentre height of the longtime-averaged pressure drag from the urban canopy, and z_0 is determined via curve fitting. More specifically,

$$d = \frac{\int_0^h \langle \bar{D} \rangle_l(x_3) x_3 \, dx_3}{\int_0^h \langle \bar{D} \rangle_l(x_3) \, dx_3}, \tag{3.2}$$

Mean flow and turbulence in unsteady canopy layers

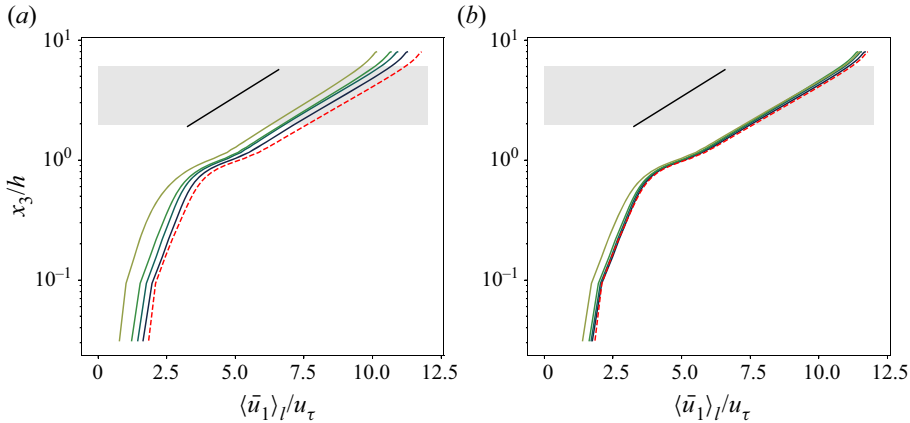


Figure 5. Wall-normal profiles of long-time-averaged streamwise velocity $\langle \bar{u}_1 \rangle_l$ of high-amplitude cases (a) and low-amplitude cases (b). Line colour specifies the forcing frequency: navy blue, $\omega T_h = 0.05\pi$; dark green, $\omega T_h = 0.125\pi$; light green, $\omega T_h = 0.25\pi$; yellow-green, $\omega T_h = 1.25\pi$. Here $\langle \bar{u}_1 \rangle_l$ from the SS case, represented by the red dashed line, is included for comparison. Black solid line indicates the slope of $1/\kappa$, with $\kappa = 0.4$. The shaded area highlights the fitting region for the estimation of the roughness length scale z_0 .

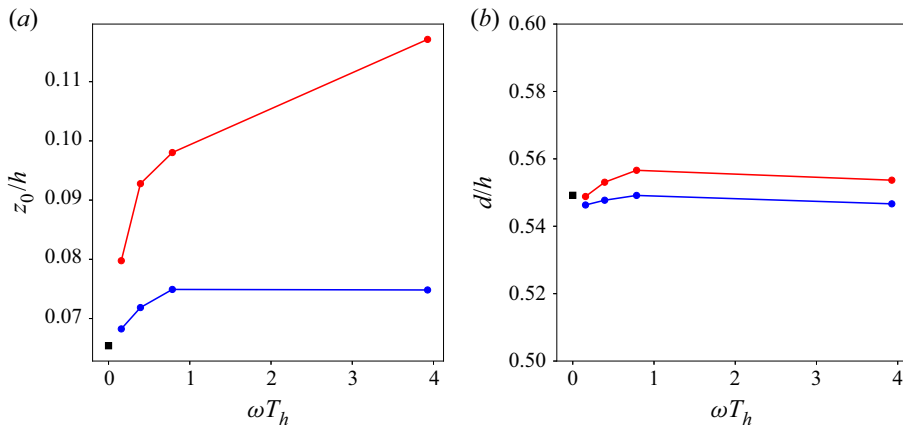


Figure 6. Normalized aerodynamic roughness length z_0 (a) and displacement height d (b). Different colours correspond to different oscillation amplitudes: blue, $\alpha = 0.2$; red, $\alpha = 0.4$. The black square symbol denotes the reference SS case.

where the wall-normal distribution of the instantaneous canopy pressure drag D is obtained by taking an intrinsic volume average of the pressure gradient, i.e.

$$D(x_3, t) = \frac{1}{V_f} \int_{x_3-\delta z/2}^{x_3+\delta z/2} \int_0^{L_2} \int_0^{L_1} \frac{1}{\rho} \frac{\partial p}{\partial x} dx_1 dx_2 dx_3. \tag{3.3}$$

Note that, in principle, one should also account for the SGS drag contribution in (3.3); in this work, we omit SGS contributions because they are negligible when compared with the total drag – a direct result of the relatively small aerodynamic roughness length that is prescribed in the wall-layer model (see § 2.1).

Here z_0 is solved by minimizing the root mean square error between the longtime-averaged velocity and the law of the wall with $\kappa = 0.4$ in the $x_3 \in [2h, 6h]$

interval, i.e.

$$E = \left\| \langle \bar{u}_1 \rangle_l - \frac{u_\tau}{\kappa} \log \left(\frac{x_3 - d}{z_0} \right) \right\|_2. \quad (3.4)$$

The fitting interval is highlighted in [figure 5](#). The estimated z_0 was found to be poorly sensitive to variations in the fitting interval within the considered range of values. Cheng *et al.* (2007) argued that MacDonald's method is accurate when surfaces are characterized by a low packing density – a requirement that is indeed satisfied in the considered cases.

As apparent from [figure 6](#), d is poorly sensitive to variations in both α and ω (variations across cases are within the $\pm 3\%$ range). This behaviour can be explained by considering that for flows over sharp-edged obstacles, such as the ones considered herein, flow separation consistently takes place at the sharp edges, irrespective of variations in α and ω . This results in a similar net pressure distribution on the faces of the cuboids across all the considered cases. This can be readily observed in [figure 4](#). The d parameter is here evaluated as the integral of the pressure gradient field over the surface area, so the above considerations provide a physical justification for the observed behaviour. Note that this finding might not be generalizable across all possible roughness morphologies. For instance, Yu *et al.* (2022) showed that separation patterns in pulsatile flows over hemispheres feature a rather strong dependence on α and ω , yielding corresponding strong variations in d .

Contrary to d , the z_0 parameter is strongly impacted by flow unsteadiness, and its value increases with α and ω . Bhaganagar (2008) reported a similar upward shift of velocity profile in his simulations of pulsatile flow over transitionally rough surfaces at a low Reynolds number. She attributed the increase in z_0 to the resonance between the unsteady forcing and the vortices shed by roughness elements, which is induced when the forcing frequency approaches that of the vortex shedding. However, such an argument does not apply to the cases under investigation, since we observed no spurious peaks in the temporal streamwise velocity spectrum. Rather, the increase in z_0 stems from the quadratic relation between the phase-averaged canopy drag and velocity, as elaborated below.

3.2.2. Phase-averaged drag-velocity relation

The phase-averaged canopy drag $\langle \bar{D} \rangle$ and the local phase- and intrinsic-averaged velocity $\langle \bar{u}_1 \rangle$ at $x_3/h \approx 0.8$ are shown in [figure 7](#), and are representative of corresponding quantities at different heights within the UCL. Results from cases with three lower frequencies and that from the SS case cluster along a single curve, highlighting the presence of a frequency-independent one-to-one mapping between $\langle \bar{D} \rangle$ and $\langle \bar{u}_1 \rangle$. As apparent from [figure 8\(a\)](#), at these three forcing frequencies, the interaction between the wind and the canopy layer is in a state of quasiequilibrium, i.e. $\langle \bar{D} \rangle$ is in phase with $\langle \bar{u}_1 \rangle$. Moreover, the shape of the aforementioned curve generally resembles the well-known quadratic drag law, which is routinely used to parameterize the surface drag in reduced-order models for stationary flow over plant and urban canopies (Lettau 1969; Raupach 1992; Macdonald *et al.* 1998; Coceal & Belcher 2004; Katul *et al.* 2004; Poggi, Katul & Albertson 2004). This finding comes as no surprise, given the quasiequilibrium state of the $\langle \bar{D} \rangle - \langle \bar{u}_1 \rangle$ relation for the three lower forcing frequencies.

On the other hand, as shown in [figure 8\(b\)](#), results from the highest-frequency cases (LVH and HVH) exhibit an orbital pattern, which stems from the time lag between $\langle \bar{D} \rangle$ and $\langle \bar{u}_1 \rangle$. Artificially removing this time lag indeed yields a better clustering of data points from the highest-frequency cases along the quadratic drag law (see [figure 7b](#)).

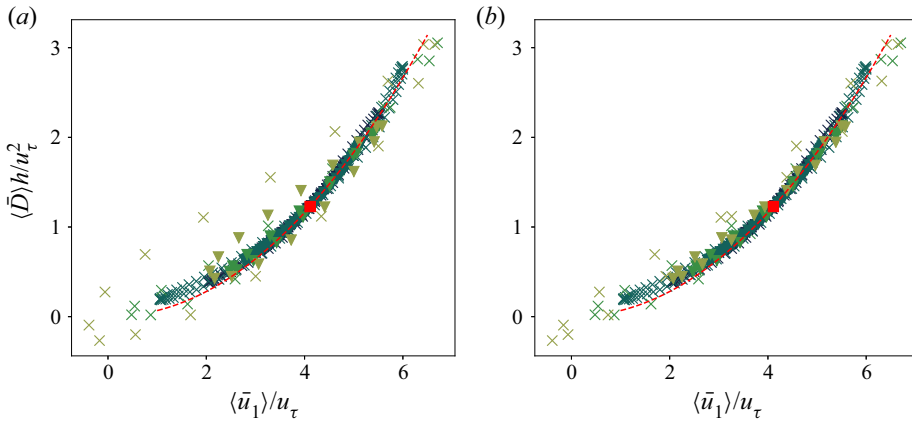


Figure 7. Phase-averaged canopy drag $\langle \bar{D} \rangle$ at $x_3/h \approx 0.8$ as a function of the local phase- and intrinsic-averaged velocity $\langle \bar{u}_1 \rangle$ (a) and the same $\langle \bar{D} \rangle - \langle \bar{u}_1 \rangle$ plot but with the time lag between $\langle \bar{D} \rangle$ and $\langle \bar{u}_1 \rangle$ removed (b). Different colours are used to denote different forcing frequencies: navy blue, $\omega T_h = 0.05\pi$; dark green, $\omega T_h = 0.125\pi$; light green, $\omega T_h = 0.25\pi$; yellow-green, $\omega T_h = 1.25\pi$. Different symbols are used to distinguish between oscillation amplitudes: triangle, $\alpha = 0.2$; cross, $\alpha = 0.4$. Red square represents the SS case. Red dashed line represents $\langle \bar{D} \rangle = C_d \lambda_f \langle \bar{u}_1 \rangle |\langle \bar{u}_1 \rangle|$ with C_d obtained from the SS case.

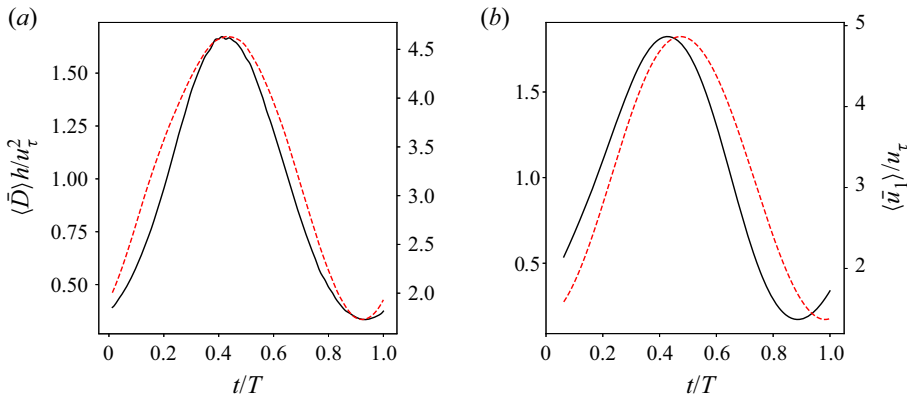


Figure 8. Time evolution of $\langle \bar{D} \rangle$ (black solid lines) and $\langle \bar{u}_1 \rangle$ (red dashed lines) at $x_3/h \approx 0.8$ from the HL (a) and LVH (b) cases. The acronyms of LES runs are defined in table 1.

These findings suggest the following parameterization for $\langle \bar{D} \rangle$:

$$\langle \bar{D} \rangle(x_3, t) = C_d(x_3) \lambda_f \langle \bar{u}_1 \rangle |\langle \bar{u}_1 \rangle| (x_3, t + \Delta t), \quad (3.5)$$

where C_d is a sectional drag coefficient that is constant in time and does not depend on α or ω , and Δt accounts for the time lag between $\langle \bar{D} \rangle$ and $\langle \bar{u}_1 \rangle$, which instead does indeed depend on α and ω . Note that, throughout the considered cases, the wall-normal-averaged drag coefficient $\int_0^h C_d dx_3/h \approx 0.9$ – a value that is similar to those previously reported ones for stationary flow over cube arrays (Coccal & Belcher 2004) (note that the exact value depends on the formula used to define C_d).

Morison, Johnson & Schaaf (1950) developed a semiempirical model relating the phase-averaged drag generated by obstacles in an oscillatory boundary layer to a given phase- and intrinsic-averaged velocity – a model that has been extensively used in the ocean engineering community to evaluate drag from surface-mounted obstacles

(Lowe, Koseff & Monismith 2005; Yu, Rosman & Hench 2018; Yu *et al.* 2022). The Morison model assumes that the total force applied to the fluid by obstacles consists of a quadratic drag term and an inertial term; the latter accounts for the added mass effect and the Froude–Krylov force arising as a direct consequence of the unsteady pressure field. While it might seem plausible to utilize the Morison model to evaluate surface drag as a function of phase-averaged velocity at a given x_3 for the cases under consideration, unfortunately, this approach is not applicable. As shown in Patel & Witz (2013), the Morison model provides relatively accurate evaluations of obstacle drag when the phased-averaged acceleration at different x_3 are in phase. This is not the case in this study, where substantial phase lags between phase-averaged accelerations at different wall-normal locations substantially degrade the accuracy of such a model. This behaviour can be easily inferred from the results in § 3.3.

In the following, we will make use of (3.5) to derive an alternative phenomenological surface-drag model for the considered flow system.

3.2.3. Mapping roughness length variability to longtime-averaged flow statistics

Here z_0 and d are input parameters of surface flux parameterizations that are routinely used in numerical weather prediction, climate projection and pollutant dispersion models (see, e.g. Skamarock *et al.* 2008; Benjamin *et al.* 2016). These models are typically based on Reynolds-averaged Navier–Stokes closures, and feature time steps that can go from one hour up to several days. When departures from stationarity occur at a time scale that is much smaller than the time step of the model, model predictions are essentially longtime-averaged quantities, and the validity of surface flux parameterizations based on flow homogeneity and stationarity assumptions may break down. As a first step towards addressing this problem, this section proposes a phenomenological model relating z_0 to longtime-averaged pulsatile-flow statistics.

The longtime-averaged friction velocity can be written as

$$u_\tau^2 = \int_0^h \langle \bar{D} \rangle_l dx_3 = \int_0^h C_d \lambda_f \langle \overline{|\bar{u}_1|} \rangle_l dx_3, \quad (3.6)$$

where $\langle \bar{D} \rangle_l$ is the longtime-averaged surface drag. Note that the wall-normal structure of C_d is approximately constant in the UCL (not shown here), except in the vicinity of the surface, where local contributions to the overall drag are, however, minimal due to the small value of $\langle \bar{u}_1 \rangle$. Thus, it is reasonable to assume C_d is constant along the wall-normal direction. Also, depending on α and ω , the flow within the canopy might undergo a local reversal in the phase- and intrinsic-averaged sense, meaning that $\langle \bar{u}_1 \rangle < 0$ at selected x_3 locations. Assuming that there is no flow reversal within the UCL, i.e. $\langle \bar{u}_1 \rangle \geq 0$ in $x_3 \leq h$, (3.6) can be written as

$$u_\tau^2 = C_d \lambda_f \left(\int_0^h \langle \bar{u}_1 \rangle_l^2 dx_3 + \int_0^h \langle \overline{|\bar{u}_1|} \rangle_l dx_3 \right), \quad (3.7)$$

where the second term on the right-hand side of (3.7) is identically zero for the SS case. Equation (3.7) essentially states that an unsteady canopy layer requires a lower longtime-averaged wind speed to generate the same drag of a steady canopy layer since quadratic drag contributions are generated by flow unsteadiness (the second term on the right-hand side of (3.7)). Note that $\sqrt{\int_0^h (\cdot)^2 dx_3 / h}$ is an averaging operation over the UCL

based on the L_2 norm. Rearranging terms in (3.7) leads to

$$\langle \bar{u}_1 \rangle_{l,avg} = \sqrt{\frac{u_\tau^2}{C_d \lambda_f h} - \frac{1}{h} \int_0^h \langle \langle \bar{u}_1 \rangle_o^2 \rangle_l dx_3}, \quad (3.8)$$

and

$$\langle \bar{u}_1 \rangle_{l,avg}^{SS} = \sqrt{\frac{u_\tau^2}{C_d \lambda_f h}}, \quad (3.9)$$

for the pulsatile cases and the SS case, respectively. Here $(\cdot)_{avg}$ denotes the canopy-averaged quantity, and $(\cdot)^{SS}$ represents a quantity pertaining to the SS case.

As discussed in § 3.2.1, flow unsteadiness yields a shift of the $\langle \bar{u}_1 \rangle_l$ profile with negligible variations in the d parameters when compared with the stationary flow with the same u_τ . In terms of the law-of-the-wall, this behaviour can be described as a variation in z_0 , i.e.

$$\langle \bar{u}_1 \rangle_{l,avg}^{SS} - \langle \bar{u}_1 \rangle_{l,avg} = \frac{u_\tau}{\kappa} \log \left(\frac{x_3 - d}{z_0^{SS}} \right) - \frac{u_\tau}{\kappa} \log \left(\frac{x_3 - d}{z_0} \right), \quad (3.10)$$

where (3.10) is valid for any x_3 in the logarithmic region. The shift in the velocity profile is approximately constant for $x_3 \in [0, L_3]$, so one can write

$$\langle \bar{u}_1 \rangle_l^{SS} - \langle \bar{u}_1 \rangle_l \approx \langle \bar{u}_1 \rangle_{l,avg}^{SS} - \langle \bar{u}_1 \rangle_{l,avg}, \quad (3.11)$$

and substituting (3.8)–(3.10) into (3.11) finally yields

$$z_0 = z_0^{SS} \exp \left[\kappa \left(\sqrt{\frac{1}{C_d \lambda_f h}} - \sqrt{\frac{1}{C_d \lambda_f h} - \frac{\int_0^h \langle \langle \bar{u}_1 \rangle_o^2 \rangle_l dx_3 / h}{u_\tau^2}} \right) \right]. \quad (3.12)$$

Equation (3.12) is a diagnostic model relating variations in the z_0 parameter to the UCL phase- and intrinsic-averaged velocity variance – a longtime-averaged quantity. The z_0 estimates from (3.12) are compared with LES results in figure 9, using $C_d = 0.9$. It is apparent that the proposed model is able to accurately evaluate z_0 for most of the considered cases. For the LVH, HH and HVW runs, z_0 is overestimated by the model; these departures are attributed to the presence of flow reversal in the UCL, which contradicts the model assumptions.

Equation (3.12) highlights that, in the absence of flow reversal, z_0 can be described as a monotonically increasing function of the $\langle \bar{u}_1 \rangle_o$ variance in the UCL. As explained at the beginning of this section, this finding is of high relevance from a flow modelling perspective, because it relates a longtime-averaged flow statistic to the z_0 parameter. Note that z_0^{SS} can be accurately evaluated using any existing parameterization for stationary ABL flow over aerodynamically rough surfaces, including the Lettau (1969), Raupach (1992) and Macdonald *et al.* (1998) models. Further, $C_d = 0.9$ (see discussion in § 3.2.2) and λ_f and h are morphological parameters that are in general *a priori* available. In weather forecasting and climate models, $\langle \bar{u}_1 \rangle_o$ is an SGS quantity and would hence have to be parameterized as a function of longtime-averaged statistics that the model computes or from available in-situ and remote sensing measurements.

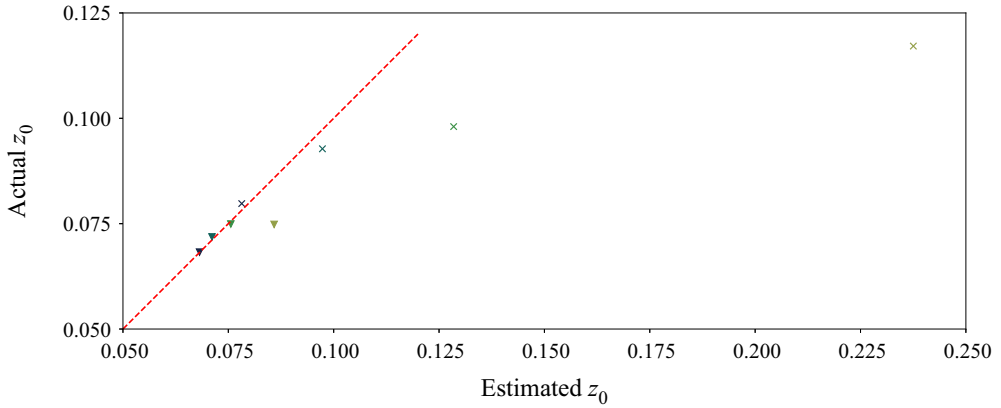


Figure 9. Comparison between z_0 estimated via (3.12) and z_0 from LES. Symbols and colours correspond to those used in figure 7.

3.2.4. Longtime-averaged resolved Reynolds stress

This section shifts the attention to longtime-averaged resolved Reynolds stresses. For all of the considered cases, contributions from SGS stresses account for $< 1\%$ of the total phase-averaged Reynolds stresses and are hence not discussed.

Throughout the boundary layer, $\langle u'_1 u'_3 \rangle_l$ profiles are indistinguishable from the SS one (not shown), indicating a weak dependence of such a quantity on α and ω . Above the UCL, the divergence of $\langle u'_1 u'_3 \rangle_l$ balances the longtime-averaged driving pressure gradient f_m , i.e.

$$-\frac{\partial \langle u'_1 u'_3 \rangle_l}{\partial x_3} + f_m = 0. \tag{3.13}$$

Since f_m does not vary across the considered cases and $\langle u'_1 u'_3 \rangle_l(L_3) = 0$, a collapse of $\langle u'_1 u'_3 \rangle_l$ profiles in this region was to be expected from the mathematical structure of the governing equations. Within the UCL, the longtime-averaged momentum budget reads

$$-\frac{\partial \langle u'_1 u'_3 \rangle_l}{\partial x_3} + f_m - \langle \bar{D} \rangle_l = 0. \tag{3.14}$$

Given that $\langle u'_1 u'_3 \rangle_l$ profiles collapse in this region, $\langle \bar{D} \rangle_l$ is also expected to feature a weak dependence on α and ω , which in turn explains the weak variations in the d parameter that were observed in § 3.2.1.

Figure 10 depicts wall-normal profiles of the longtime-averaged resolved turbulent kinetic energy, which is defined as

$$\langle \bar{k} \rangle_l = \frac{1}{2} (\langle u'_1 u'_1 \rangle_l + \langle u'_2 u'_2 \rangle_l + \langle u'_3 u'_3 \rangle_l). \tag{3.15}$$

Such a quantity features a significant increase in the UCL when compared with its values farther away from the surface, which as discussed in Schmid *et al.* (2019), is due to dispersive contributions caused by the canopy geometry. Flow unsteadiness has a relatively more important impact on such a quantity when compared with the $\langle u'_1 u'_3 \rangle_l$ component, especially for flow in the UCL and for cases with a high oscillation amplitude. An increase in α generally results in more pronounced departures of $\langle \bar{k} \rangle_l$ profiles from the SS one.

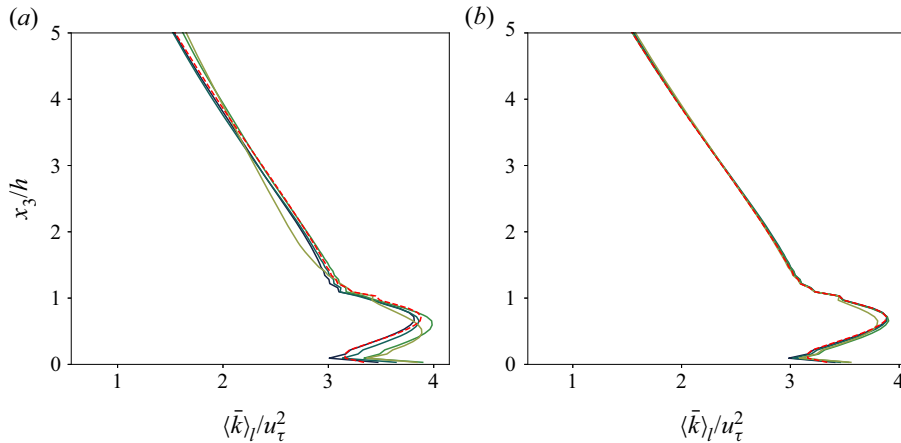


Figure 10. Longtime-averaged resolved turbulent kinetic energy $\langle \bar{k} \rangle_l = (\overline{\langle u'_1 u'_1 \rangle_l} + \overline{\langle u'_2 u'_2 \rangle_l} + \overline{\langle u'_3 u'_3 \rangle_l})/2$ from high-amplitude cases (a) and low-amplitude cases (b). Line colours correspond to those used in figure 5.

This behaviour can be best explained by considering the shear production terms in the budget equation for $\langle \bar{k} \rangle_l$, i.e.

$$\langle \bar{\mathcal{P}} \rangle_l = - \left\langle \overline{\langle u'_1 u'_3 \rangle} \frac{\partial \langle \bar{u}_1 \rangle}{\partial x_3} \right\rangle_l = \underbrace{- \langle \overline{\langle u'_1 u'_3 \rangle_l} \frac{\partial \langle \bar{u}_1 \rangle_l}{\partial x_3} \rangle_l}_{\langle \bar{\mathcal{P}} \rangle_{l,1}} - \underbrace{\left\langle \overline{\langle u'_1 u'_3 \rangle_o} \frac{\partial \langle \bar{u}_1 \rangle_o}{\partial x_3} \right\rangle_l}_{\langle \bar{\mathcal{P}} \rangle_{l,2}}, \quad (3.16)$$

where $\langle \bar{\mathcal{P}} \rangle_{l,1}$ represents the work done by $\overline{\langle u'_1 u'_3 \rangle_l}$ onto the longtime-averaged flow field, and $\langle \bar{\mathcal{P}} \rangle_{l,2}$ is the longtime average of the work done by the oscillatory shear stress $\overline{\langle u'_1 u'_3 \rangle_o}$ onto the oscillatory flow field. Figure 11(a) shows that $\langle \bar{\mathcal{P}} \rangle_{l,1}$ is poorly sensitive to variations in α and ω . This behaviour stems from the constancy of $\overline{\langle u'_1 u'_3 \rangle_l}$ and $\partial \langle \bar{u}_1 \rangle_l / \partial x_3$ across cases (the latter can be inferred from the systematic shift of $\langle \bar{u}_1 \rangle_l$ profiles in figure 5). Conversely, $\langle \bar{\mathcal{P}} \rangle_{l,2}$ from high-amplitude cases are generally larger than those from low-amplitude ones, mainly due to the higher $\overline{\langle u'_1 u'_3 \rangle_o}$ and $\langle \bar{u}_1 \rangle_o$ values. Discrepancies in $\langle \bar{\mathcal{P}} \rangle_{l,2}$ among high-amplitude cases are larger than those among low-amplitude ones, which ultimately yields the observed variability in $\langle \bar{k} \rangle_l$.

Further insight into the problem can be gained by looking at the normal components of the longtime-averaged resolved Reynolds stress tensor, which are shown in figure 12. In this case, it is apparent that increases in the oscillation frequency lead to a decrease in $\overline{\langle u'_1 u'_1 \rangle_l}$ and an increase in $\overline{\langle u'_2 u'_2 \rangle_l}$ and $\overline{\langle u'_3 u'_3 \rangle_l}$ within the UCL – a behaviour that is especially apparent for the high-amplitude cases (figure 12d–f). These trends can be best understood by examining the pressure-strain terms from the budget equations of the longtime-averaged resolved Reynolds stresses, i.e.

$$R_{ij} = \left\langle \frac{p'}{\rho} \left(\frac{\partial u'_j}{\partial x_i} + \frac{\partial u'_i}{\partial x_j} \right) \right\rangle_l. \quad (3.17)$$

Here R_{ij} are responsible for redistributing kinetic energy among the longtime-averaged normal Reynolds stresses (Pope 2000), and are shown in figure 13. With the exception of

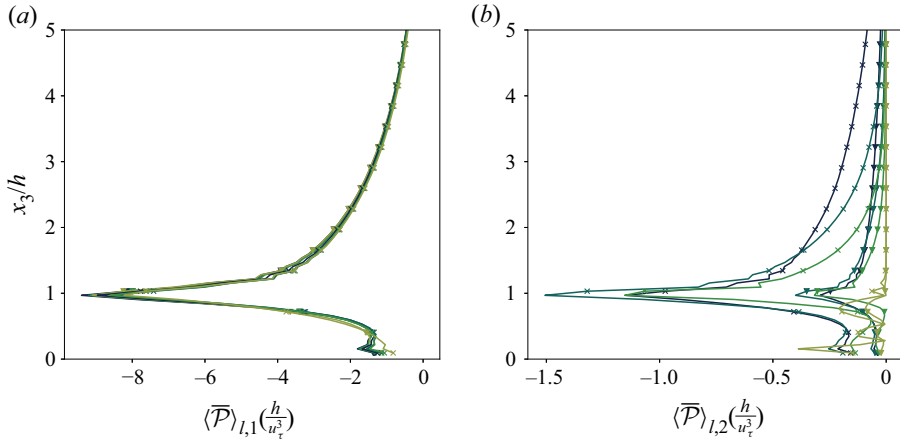


Figure 11. Normalized shear production terms of $\langle \bar{k} \rangle_l$: $\langle \bar{\mathcal{P}} \rangle_{l,1}$ (a) and $\langle \bar{\mathcal{P}} \rangle_{l,2}$ (b). Symbols and line colours correspond to those used in figure 7.

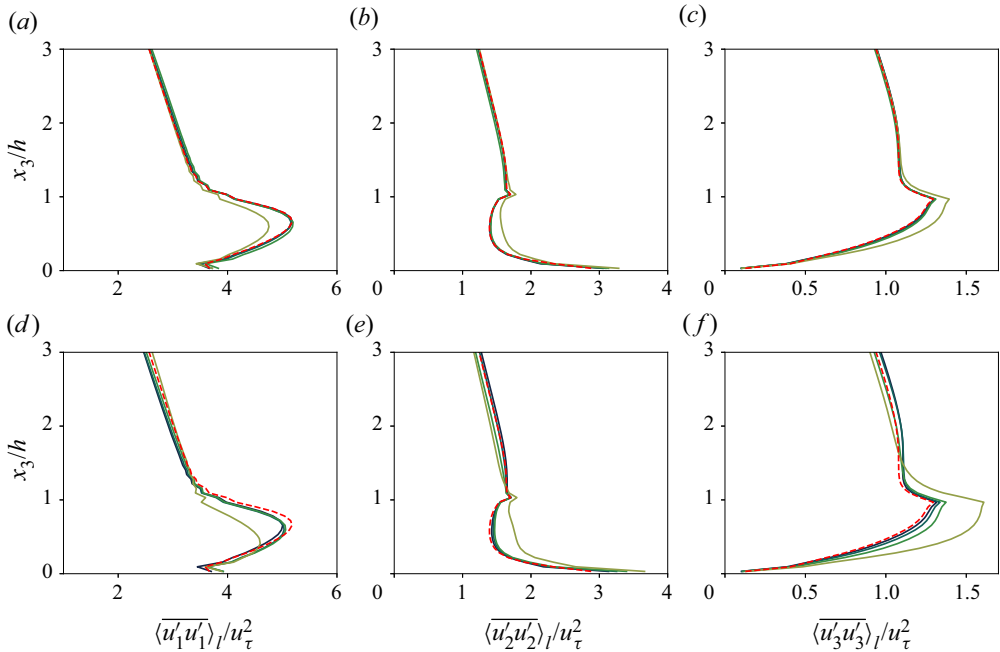


Figure 12. Longtime-averaged resolved normal Reynolds stresses $\langle \overline{u'_1 u'_1} \rangle_l$, $\langle \overline{u'_2 u'_2} \rangle_l$ and $\langle \overline{u'_3 u'_3} \rangle_l$ from low-amplitude cases (a–c) and high-amplitude cases (d–f). Line colours correspond to those used in figure 5.

the very near surface region ($x_3 \lesssim 0.2$) where no clear trend can be observed, increases in ω and α yield a decrease in R_{11} and an increase in R_{22} and R_{33} , which justify the observed isotropization of turbulence in the UCL.

3.3. Oscillatory fields

This section shifts the focus to the time evolution of velocity and resolved Reynolds stresses during the pulsatile cycle.

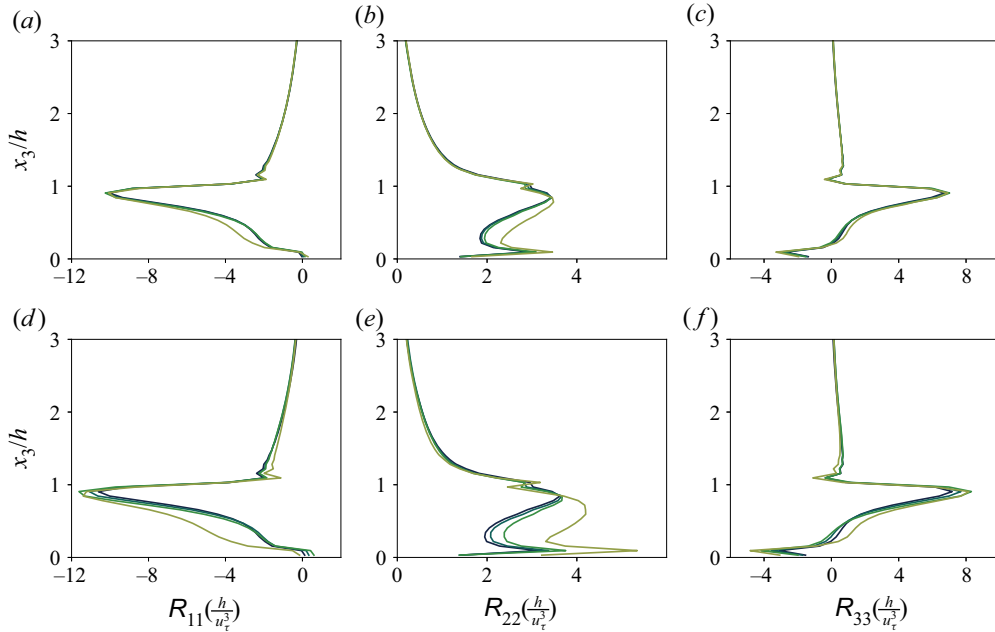


Figure 13. Pressure redistribution terms R_{ii} : (a–c) low-amplitude cases; (d–f) high-amplitude cases. Line colours correspond to those used in figure 5.

3.3.1. Oscillation amplitude impacts on the oscillatory fields

Flow statistics from the LL and HL simulations are here examined to study the impact of the oscillation amplitude (α) on the oscillatory velocity and resolved Reynolds stresses. Only the LL and HL runs are discussed, as they were found to be representative of the observed behaviours for the other low and high-amplitude cases, respectively.

Figure 14 contrasts the profiles of oscillatory velocity ($\langle \bar{u}_1 \rangle_o$) from the LL and HL runs at four equispaced phases during the pulsatile cycle. The $\langle \bar{u}_1 \rangle_o$ at the top of the domain is controlled by the α parameter, so it is natural to use $u_\tau \alpha$ as a normalization constant to study the problem. Manna *et al.* (2012) investigated pulsatile open channel flow over an aerodynamically smooth surface, and showed that using such a normalization constant is indeed convenient as it leads to a collapse of $\langle \bar{u}_1 \rangle_o$ profiles across cases with different amplitudes, even in the presence of strong flow reversal. This indicates that, at a given forcing frequency, the amplitude of the oscillatory velocity within the domain is proportional to that at the top of the domain. In this work, we show that such a scaling works well also in the presence of aerodynamically rough surfaces, as evidenced by the excellent collapse of $\langle \bar{u}_1 \rangle_o / (u_\tau \alpha)$ profiles in figure 14. This is not trivial, especially when considering the different scaling of surface drag between aerodynamically smooth and rough walls in the presence of flow unsteadiness.

The oscillatory resolved turbulent kinetic energy can be defined as

$$\langle \bar{k} \rangle_o = \frac{1}{2} (\langle \bar{u}'_1 u'_1 \rangle_o + \langle \bar{u}'_2 u'_2 \rangle_o + \langle \bar{u}'_3 u'_3 \rangle_o). \quad (3.18)$$

As shown in figures 15 and 16, both the oscillatory resolved Reynolds shear stress $\langle \bar{u}'_1 u'_3 \rangle_o$ and $\langle \bar{k} \rangle_o$ scale with $u_\tau^2 \alpha$. Although not shown, the three oscillatory normal Reynolds stresses also obey such a scaling, suggesting that any change in $\langle \bar{k} \rangle_o$ is proportionally distributed to the three normal Reynolds stresses during the pulsatile cycle. As discussed

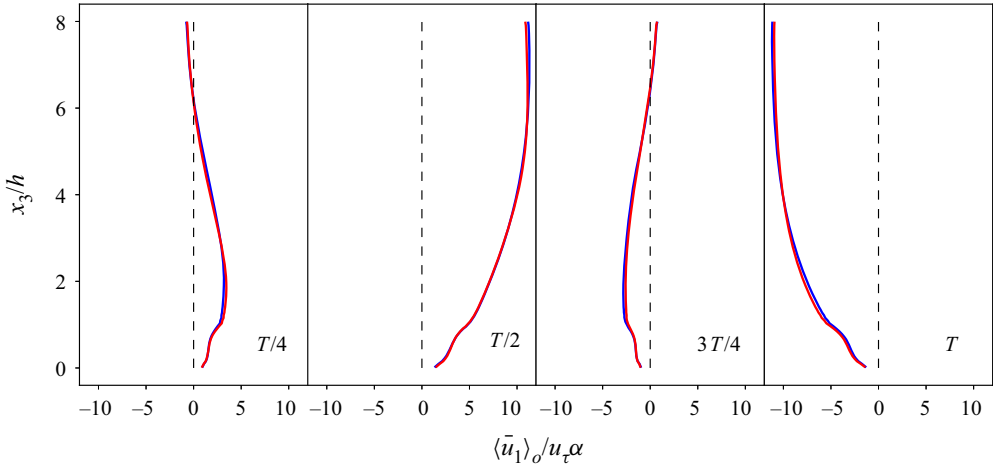


Figure 14. Profiles of the oscillatory velocity $\langle \bar{u}_1 \rangle_o$ from the LL (blue) and HL (red) cases at different phases of the pulsatile cycle. Profiles are $T/4$ apart.

in the following paragraphs, the scaling of $\langle \overline{u'_1 u'_3} \rangle_o$ and $\langle \bar{k} \rangle_o$ is a direct consequence of the mild nonlinearity in the production of $\langle \bar{k} \rangle_o$ and $\langle \overline{u'_1 u'_3} \rangle_o$. Subtracting the budget equation of $\langle \overline{u'_1 u'_3} \rangle_l$ from that of $\langle \overline{u'_1 u'_3} \rangle_o$, one obtains

$$\begin{aligned} \frac{\partial \langle \overline{u'_1 u'_3} \rangle_o}{\partial t} &= \underbrace{-2 \langle \overline{u'_3 u'_3} \rangle_o \frac{\partial \langle \bar{u}_1 \rangle_l}{\partial x_3}}_{\langle \bar{\mathcal{P}}_{13} \rangle_{o,l1}} - \underbrace{2 \langle \overline{u'_3 u'_3} \rangle_l \frac{\partial \langle \bar{u}_1 \rangle_o}{\partial x_3}}_{\langle \bar{\mathcal{P}}_{13} \rangle_{o,l2}} \\ &\quad - \underbrace{2 \langle \overline{u'_3 u'_3} \rangle_o \frac{\partial \langle \bar{u}_1 \rangle_o}{\partial x_3} + 2 \left\langle \overline{\langle \overline{u'_3 u'_3} \rangle_o \frac{\partial \langle \bar{u}_1 \rangle_o}{\partial x_3}} \right\rangle_l}_{\langle \bar{\mathcal{P}}_{13} \rangle_{o,nl}} + \dots, \end{aligned} \quad (3.19)$$

where $\langle \bar{\mathcal{P}}_{13} \rangle_{o,l1}$ and $\langle \bar{\mathcal{P}}_{13} \rangle_{o,l2}$ are the linear production terms of $\langle \overline{u'_1 u'_3} \rangle_o$, while $\langle \bar{\mathcal{P}}_{13} \rangle_{o,nl}$ is the nonlinear production. Similarly, the budget equations of $\langle \bar{k} \rangle_o$ can be written as

$$\frac{\partial \langle \bar{k} \rangle_o}{\partial t} = \underbrace{-\langle \overline{u'_1 u'_3} \rangle_o \frac{\partial \langle \bar{u}_1 \rangle_l}{\partial x_3}}_{\langle \bar{\mathcal{P}}_k \rangle_{o,l1}} - \underbrace{\langle \overline{u'_1 u'_3} \rangle_l \frac{\partial \langle \bar{u}_1 \rangle_o}{\partial x_3}}_{\langle \bar{\mathcal{P}}_k \rangle_{o,l2}} - \underbrace{\langle \overline{u'_1 u'_3} \rangle_o \frac{\partial \langle \bar{u}_1 \rangle_o}{\partial x_3} + \left\langle \overline{\langle \overline{u'_1 u'_3} \rangle_o \frac{\partial \langle \bar{u}_1 \rangle_o}{\partial x_3}} \right\rangle_l}_{\langle \bar{\mathcal{P}}_k \rangle_{o,nl}} + \dots, \quad (3.20)$$

where $\langle \bar{\mathcal{P}}_k \rangle_{o,l1}$ and $\langle \bar{\mathcal{P}}_k \rangle_{o,l2}$ are the linear production terms of $\langle \bar{k} \rangle_o$, while $\langle \bar{\mathcal{P}}_k \rangle_{o,nl}$ is the nonlinear production. As shown in figure 17, the nonlinear production term is substantially smaller than the sum of the corresponding linear productions for both $\langle \overline{u'_1 u'_3} \rangle_o$ and $\langle \bar{k} \rangle_o$. Given that $\langle \overline{u'_1 u'_3} \rangle_l$, $\langle \overline{u'_3 u'_3} \rangle_l$ and $\partial \langle \bar{u}_1 \rangle_l / \partial x_3$ from the LL and HL cases are similar, when $\langle \bar{u}_1 \rangle_o \sim u_\tau \alpha$ and $\langle \overline{u'_3 u'_3} \rangle_o \sim u_\tau^2 \alpha$, the total production of $\langle \overline{u'_1 u'_3} \rangle_o$ is

$$\langle \bar{\mathcal{P}}_{13} \rangle_o \approx \langle \bar{\mathcal{P}}_{13} \rangle_{o,l1} + \langle \bar{\mathcal{P}}_{13} \rangle_{o,l2} \sim \frac{u_\tau^3 \alpha}{h}, \quad (3.21)$$

Mean flow and turbulence in unsteady canopy layers

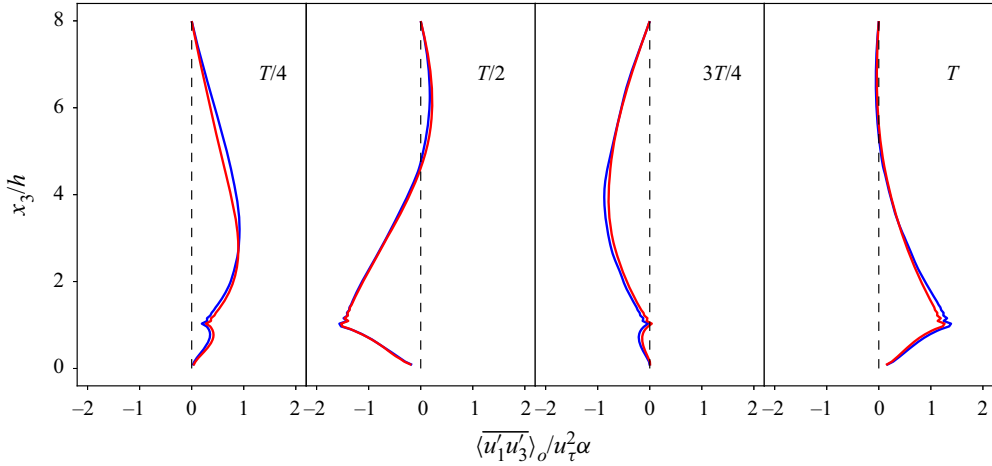


Figure 15. Profiles of the oscillatory resolved Reynolds shear stress $\langle u'_1 u'_3 \rangle_o$ from the LL (blue) and HL (red) cases at different phases of the pulsatile cycle. Profiles are $T/4$ apart.

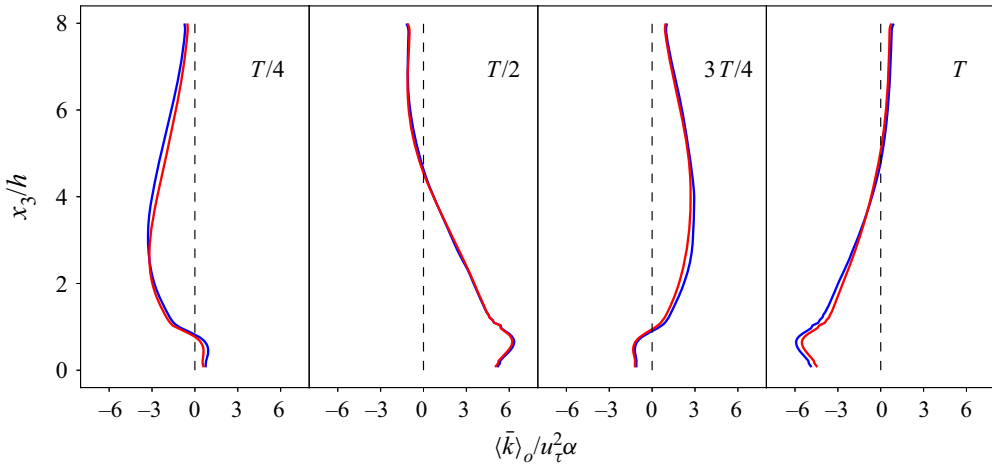


Figure 16. Profiles of the oscillatory resolved turbulent kinetic energy $\langle \bar{k} \rangle_o = (\langle u'_1 u'_1 \rangle_o + \langle u'_2 u'_2 \rangle_o + \langle u'_3 u'_3 \rangle_o) / 2$ from the LL (blue) and HL (red) cases at different phases of the pulsatile cycle. Profiles are $T/4$ apart.

whereas that of $\langle \bar{k} \rangle_o$ is

$$\langle \bar{\mathcal{P}}_k \rangle_o \approx \langle \bar{\mathcal{P}}_k \rangle_{o,11} + \langle \bar{\mathcal{P}}_k \rangle_{o,12} \sim \frac{u_\tau^3 \alpha}{h}. \quad (3.22)$$

This in turn leads to the observed $\langle u'_1 u'_3 \rangle_o \sim u_\tau^2 \alpha$ and $\langle \bar{k} \rangle_o \sim u_\tau^2 \alpha$ scalings.

Equations (3.21) and (3.22) are expected to fail under two conditions. Firstly, when α is sufficiently large and the contribution of $\langle \bar{\mathcal{P}}_{13} \rangle_{o,nl}$ and $\langle \bar{\mathcal{P}}_k \rangle_{o,nl}$ can no longer be neglected. Secondly, when differences in $\langle u'_1 u'_3 \rangle_l$ or $\langle u'_3 u'_3 \rangle_l$ among cases with different α become large enough that the linear production terms cease to scale with $u_\tau^2 \alpha$, which occurs within the UCL for the LVH and HVH cases (see figure 12).

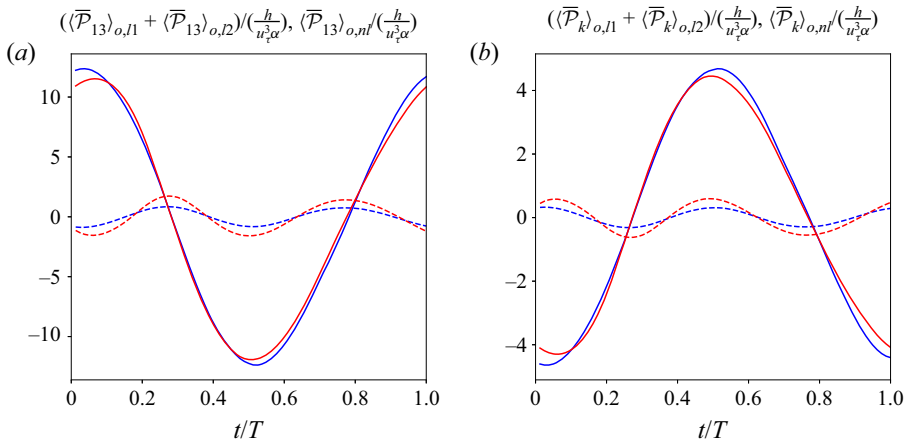


Figure 17. Normalized production terms for $\langle \bar{u}'_1 \bar{u}'_3 \rangle_o$ (a) and for $\langle \bar{k} \rangle_o$ (b) at $x_3/h = 1.5$ from the LL (blue) and HL (red) cases. Solid lines denote the linear production terms, and dash lines represent the nonlinear production terms.

The above analysis has shown that the α parameter primarily controls the amplitude of selected oscillatory flow quantities, but has little impact on their wall-normal structure. In the next section, it will be shown that the wall-normal structure of quantities is instead controlled by ω . This behaviour is also expected to hold in the smooth-wall set-up (Manna *et al.* 2012), although the mechanism responsible for generating drag over aerodynamically smooth surfaces is quite distinct.

3.3.2. Forcing frequency impacts on the oscillatory fields

This section discusses how the oscillatory velocity and resolved Reynolds stresses respond to variations in the forcing frequency. Only low-amplitude cases will be considered since conclusions can be generalized across the considered runs.

Figures 18 and 19 present the time evolution of $\langle \bar{u}_1 \rangle_o$ and $\partial \langle \bar{u}_1 \rangle_o / \partial x_3$. Three distinct frequency regimes can be identified. The first regime corresponds to the highest amongst the considered forcing frequencies, i.e. the LVH case. For this flow regime, the oscillation in $\partial \langle \bar{u}_1 \rangle_o / \partial x_3$ is typically confined within the UCL. This behaviour can be best explained when considering that the time period of the oscillation is comparable to the eddy turnover time of turbulence in the UCL, i.e. $T \approx T_h$, which is the characteristic time scale for ‘information transport’ within the UCL. At the three lower forcing frequencies, i.e. the LL, LM and LH cases, on the contrary, the interaction between the roughness elements and the unsteady flow induces an oscillation in the shear rate, which has a phase lag of roughly $\pi/2$ with respect to the pulsatile forcing at the top of the UCL. This oscillating shear rate then propagates in the positive wall-normal direction while being progressively attenuated. The propagation speed of the oscillating shear rate appears to be constant for a given forcing frequency, which can be readily inferred by the constant tilting angle in the $\partial \langle \bar{u}_1 \rangle_o / \partial x_3$ contours. The flow region affected by the oscillating shear rate defines the so-called ‘Stokes layer’. For cases with two moderate frequencies, i.e. the LM and LH cases, the Stokes layer thickness (δ_s) is smaller than the domain height L_3 . Above the Stokes layer, the slope of $\langle \bar{u}_1 \rangle_o$ is nominally zero over the pulsatile cycle, and the flow in such a region resembles a plug flow. On the contrary, in the LL case, the entire domain is affected by the oscillating shear rate, thus $\delta_s > L_3$.

Mean flow and turbulence in unsteady canopy layers

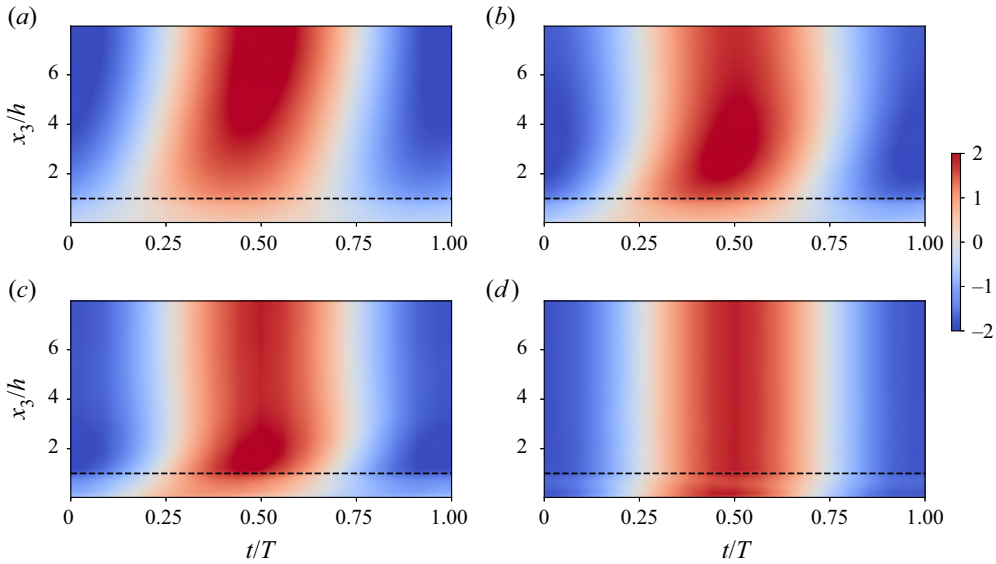


Figure 18. Space–time diagrams of $\langle \bar{u}_1 \rangle_o / u_\tau$ from the LL (a), LM (b), LH (c) and LVH (d) cases. Horizontal dashed lines identify the top of the UCL.

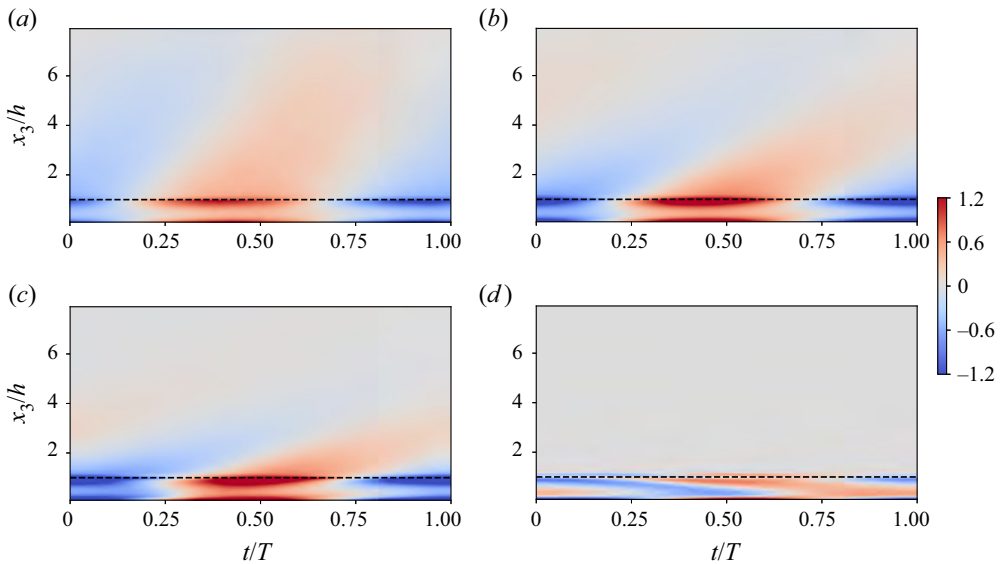


Figure 19. Space–time diagrams of $(h/u_\tau) \partial \langle \bar{u}_1 \rangle_o / \partial x_3$ from the LL (a), LM (b), LH (c) and LVH (d) cases.

Figures 20 and 21 depict the time evolution of $\overline{\langle u'_1 u'_3 \rangle}_o$ and $\overline{\langle u'_1 u'_1 \rangle}_o$, respectively. Although the contours of $\overline{\langle u'_2 u'_2 \rangle}_o$ and $\overline{\langle u'_3 u'_3 \rangle}_o$ are not shown, these quantities vary in a similar fashion as $\overline{\langle u'_1 u'_1 \rangle}_o$ during the pulsatile cycle. These space–time diagrams confirm that the considered frequencies encompass three distinct flow regimes. For the LVH case, time variations of the oscillatory resolved Reynolds stresses are essentially zero above the UCL. In cases with three lower frequencies, oscillatory resolved Reynolds stresses exhibit

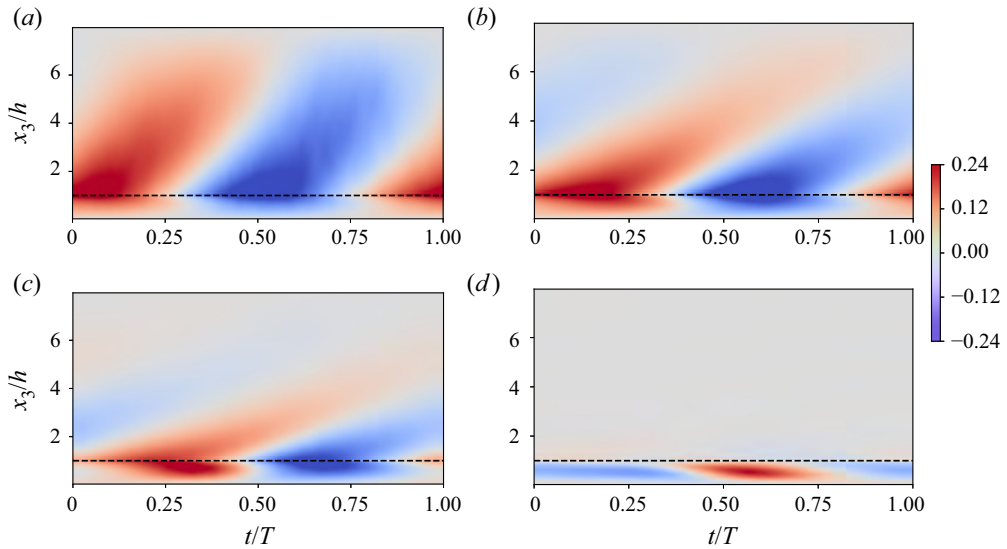


Figure 20. Space-time diagrams of $\langle \overline{u_1' u_3'} \rangle_o / u_\tau^2$ from the LL (a), LM (b), LH (c) and LVH (d) cases.

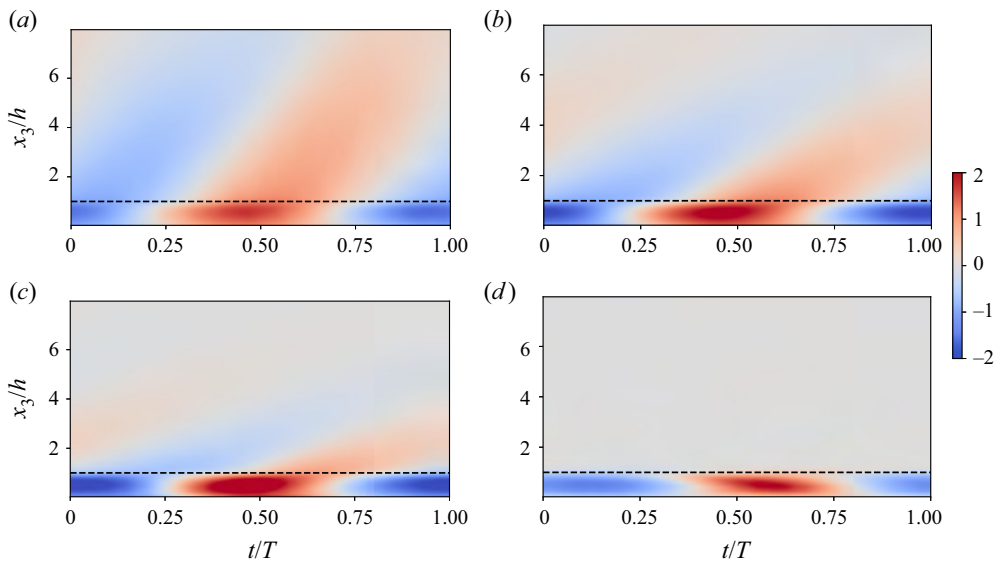


Figure 21. Space-time diagrams of $\langle \overline{u_1' u_1'} \rangle_o / u_\tau^2$ from the LL (a), LM (b), LH (c) and LVH (d) cases.

a similar behaviour to $\partial \langle \overline{u_1} \rangle_o / \partial x_3$. Specifically, there appear oscillating waves propagating away from the UCL at a constant speed and meanwhile getting weakened. In the LM and LH cases, such oscillating waves are fully dissipated at the upper limit of the Stokes layer, above which the turbulence is ‘frozen’ and passively advected.

A visual comparison of the tilting angles in the contours of oscillatory resolved Reynolds stresses and $\partial \langle \overline{u_1} \rangle_o / \partial x_3$ reveals that the oscillating waves in these quantities feature similar propagation speeds. This behaviour closely resembles the one observed in smooth-wall cases (Scotti & Piomelli 2001; Manna *et al.* 2015). The physical interpretation is that when the oscillating shear rate is diffused upwards by the background turbulent flow, it

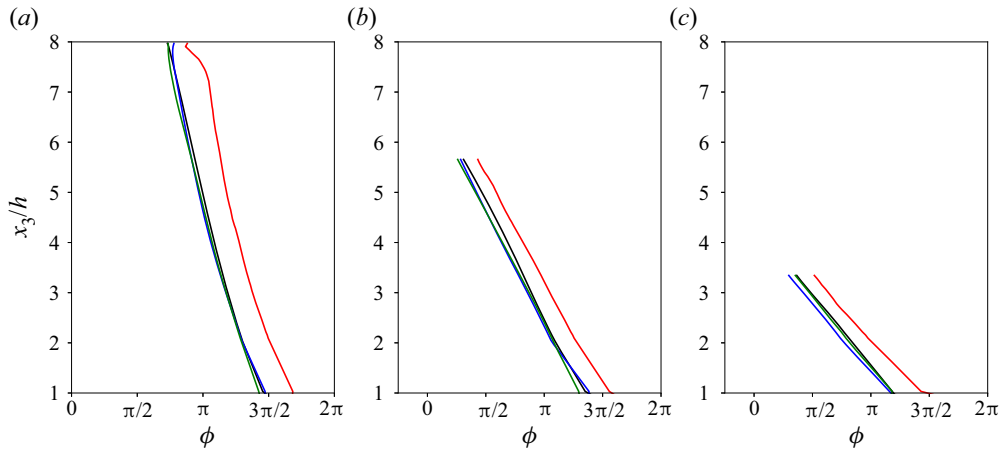


Figure 22. Phase lag of $\partial\langle\bar{u}_1\rangle_o/\partial x_3$ (red), $-\langle u'_1u'_3\rangle_o$ (black), $\langle u'_1u'_1\rangle_o$ (magenta), $\langle u'_2u'_2\rangle_o$ (green) and $\langle u'_3u'_3\rangle_o$ (blue) with respect to the pulsatile forcing from the LL (a), LM (b) and LH (c) cases.

Case	c_{du1dx3}/u_τ	c_{-u1u3}/u_τ	c_{u1u1}/u_τ	c_{u2u2}/u_τ	c_{u3u3}/u_τ
LL	0.50	0.51	0.51	0.49	0.48
LM	0.55	0.54	0.60	0.57	0.58
LH	0.72	0.71	0.77	0.76	0.74

Table 2. Propagation speeds of oscillating waves in $\partial\langle\bar{u}_1\rangle_o/\partial x_3$ and oscillatory resolved Reynolds stresses.

interacts with the local turbulence via the mechanisms described in (3.19) and (3.20), thus inducing the observed oscillations in the resolved Reynolds stresses. To further quantify the propagation speeds of the oscillating waves in $\partial\langle\bar{u}_1\rangle_o/\partial x_3$ and oscillatory resolved Reynolds stresses, figure 22 presents the phase lag of those quantities with respect to the pulsatile forcing. For a quantity θ , the propagation speed c_θ is defined based on the slope of the phase lag, i.e.

$$c_\theta = -\omega \frac{\partial x_3}{\partial \phi_\theta}. \quad (3.23)$$

Table 2 summarizes the wave propagation speeds for $\partial\langle\bar{u}_1\rangle_o/\partial x_3$, $-\langle u'_1u'_3\rangle_o$, $\langle u'_1u'_1\rangle_o$, $\langle u'_2u'_2\rangle_o$ and $\langle u'_3u'_3\rangle_o$ of each case. This again confirms that the oscillating waves propagate at a similar speed for the considered quantities. It is also noteworthy to point out that the speed of the propagating wave increases with ω .

Three other observations can be made from figure 22. First, throughout the considered cases, there appears a marked phase lag of roughly $\pi/6$ between $\partial\langle\bar{u}_1\rangle_o/\partial x_3$ and (negative) $\langle u'_1u'_3\rangle_o$, indicating a deviation from the Boussinesq eddy viscosity assumption. Weng *et al.* (2016) reported a similar finding, and they attributed such behaviour to non-equilibrium effects arising when the time period of the pulsatile forcing is short compared with the local turbulence relaxation time so that the turbulence is not able to relax to its equilibrium state during the pulsation cycle. Second, the lack of phase lag among the oscillatory normal resolved Reynolds stresses implies that the oscillatory pressure-redistribution terms respond immediately to the change in $\langle u'_1u'_1\rangle_o$. Third, the lifetimes of oscillating

waves in the resolved Reynolds stresses and shear rate, which are inferred by the difference between the phase lags at the top of the UCL and at the upper limit of the Stokes layer, are no more than half of the oscillation time period, although they decrease with ω . They are considerably shorter than those in smooth-wall cases, which are typically larger than one oscillation period (Scotti & Piomelli 2001; Manna *et al.* 2015; Weng *et al.* 2016).

3.3.3. Scaling of the Stokes layer thickness

Across many applications, δ_s is a quantity of interest, since it defines the region where the turbulence and the mean flow are out of equilibrium. In such a region, established turbulence theories may fail to capture flow dynamics that are of relevance for, e.g. surface drag and scalar dispersion.

For the wave-current boundary flow, where the surface is typically transitionally rough, the wave boundary layer thickness – an equivalent of Stokes layer thickness – scales as

$$\delta_w \sim \frac{\kappa u_{\tau, \max}}{\omega}, \quad (3.24)$$

where $u_{\tau, \max}$ is the friction velocity based on the maximum phase- and intrinsic-averaged wall stress during the pulsatile cycle (Grant & Madsen 1979). Such a scaling argument is not valid for the current cases, even though the considered surface is also rough. As shown in § 3.3.1, normalized oscillatory velocity and resolved Reynolds stresses profiles collapse between cases with the same frequencies, implying that the Stokes layer thickness is only dependent on ω , whereas τ_{\max} is determined by both α and ω . Rather, the scaling of δ_s in the current cases is a trivial extension of the model first introduced by Scotti & Piomelli (2001), as discussed next.

Let us recall from § 1 that the Stokes layer thickness for turbulent pulsatile flow over an aerodynamically smooth surface (Scotti & Piomelli 2001) is defined as

$$\delta_s = 2 \frac{\kappa u_{\tau}}{\omega} \left(1 + \sqrt{1 + \frac{2\nu\omega}{\kappa^2 u_{\tau}^2}} \right). \quad (3.25)$$

Here we apply two modifications to this model in order to make it applicable to the current rough-wall cases. First, given that the viscous stress is omitted, the molecular viscosity ν can be neglected. Also, in the current cases, the oscillating shear rate is generated within the UCL rather than at the bottom surface (as in the smooth-wall cases), and the extent of the oscillating shear rate propagation defines the thickness of the Stokes layer. This behaviour can be easily captured by augmenting δ_s by the displacement height (d). Specifically, we draw an analogy to smooth-wall cases by taking d as the offset, since it is the virtual origin of the longtime-averaged velocity profile. The displacement height, d , is a plausible choice of the offset since it captures the limiting behaviour of the flow system as the canopy packing density varies. For instance, in the limit of $\lambda_p \rightarrow 0$ (very sparse canopies), $d = 0$, i.e. the oscillating shear rate grows from the bottom of the domain. On the contrary, in the limit of $\lambda_p \rightarrow 1$ (very dense canopies), $d = h$, i.e. the oscillating shear layer starts at the top of the UCL. Based on these considerations, a phenomenological model for the Stokes layer thickness is

$$\delta_s = \frac{4\kappa u_{\tau}}{\omega} + d. \quad (3.26)$$

Note that, in the limit of $\omega \rightarrow 0$, the Stokes layer no longer exists, rendering (3.26) invalid. At this limit, as previously stated in Scotti & Piomelli (2001), T is much larger than the

Mean flow and turbulence in unsteady canopy layers

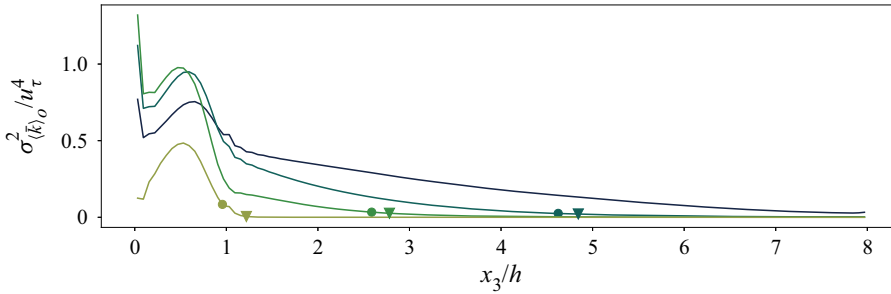


Figure 23. Time variance of $\langle \bar{k} \rangle_o$: $\sigma_{\langle \bar{k} \rangle_o}^2 = \int_0^T \left(\frac{1}{2} (\overline{u_1' u_1'})_o + \overline{u_2' u_2'}_o + \overline{u_3' u_3'}_o \right)^2 dt / T$ of the LL (navy blue), LM (dark green), LH (light green) and LVH (yellow green) cases. Circle denotes δ_s estimated via (3.26). Triangle represents the location where $\sigma_{\langle \bar{k} \rangle_o}^2$ is reduced to 1% of its maximum value.

turbulence relaxation time. As a result, the turbulence maintains a quasiequilibrium state, and the flow statistics are indistinguishable from those of the corresponding equilibrium canopy layer flows, if scaled with the instantaneous inner/outer units.

Figure 23 compares the predictions of (3.26) against LES results. Note that only low-amplitude cases are shown, since, as mentioned earlier, δ_s only depends on ω . The upper limit of the Stokes layer is identified as the location where $\sigma_{\langle \bar{k} \rangle_o}^2$ is 1% of its maximum, where

$$\sigma_{\langle \bar{k} \rangle_o}^2 = \frac{1}{T} \int_0^T \left(\frac{1}{2} (\overline{u_1' u_1'})_o + \overline{u_2' u_2'}_o + \overline{u_3' u_3'}_o \right)^2 dt \quad (3.27)$$

is the time variance of $\langle \bar{k} \rangle_o$. From figure 23, it is apparent that the estimated δ_s compare very well with LES results. The estimation of δ_s for the LL case is not shown in figure 23 because it exceeds the height of the computational domain. Equation (3.26) can hence be used in future studies to identify the Stokes layer thickness for pulsatile flows over aerodynamically rough surfaces.

4. Conclusions

This paper has examined the impact of flow pulsation on longtime-averaged and phase-dependent flow statistics in an open-channel flow over urban-like roughness. A series of LES of pulsatile flow past an array of cuboid elements has been carried out, programmatically varying the oscillation amplitude (α) and frequency (ω). The forcing frequencies have been chosen as a multiple of the characteristic frequency of turbulence in the UCL and encompass a range of values representative of submesoscale motions (Mahrt & Bou-Zeid 2020). The main findings and contributions of this study are outlined below.

- (i) Flow pulsation leads to an increase of the z_0 parameter deduced from longtime-averaged $\langle \bar{u}_1 \rangle_l$ profiles, with larger α and ω values yielding a larger z_0 . On the contrary, d was found to be insensitive to variations in α and ω . The increase of z_0 was shown to be a direct consequence of the quadratic relation between the phase-averaged canopy drag $\langle \bar{D} \rangle$ and the phase- and intrinsic-averaged velocity $\langle \bar{u}_1 \rangle$, and this relation was leveraged to construct a phenomenological model for z_0 . The proposed model takes surface information and the variance of the phase- and intrinsic-averaged velocity in the UCL as input parameters and captures the impact of flow unsteadiness on the z_0 parameter in the absence of flow reversal.

- (ii) The wall-normal distributions of the longtime-averaged shear stress and canopy drag are unaltered by the flow unsteadiness. In contrast, the same cannot be said for longtime-averaged resolved normal Reynolds stresses, especially in the UCL. In particular, $\langle \bar{k} \rangle_l$ profiles were found to be relatively more sensitive to variations in α via the longtime-averaged shear production of $\langle \bar{k} \rangle_l$. The highest frequency cases were also characterized by a relatively more isotropic turbulence field in the UCL, owing to a more efficient kinetic energy redistribution by the pressure-strain terms.
- (iii) The oscillation amplitudes of phase- and intrinsic-averaged streamwise velocity and resolved Reynolds stresses scale with α . This behaviour is due to the fact that the nonlinear production terms of $\langle \overline{u'_1 u'_3} \rangle_o$ and $\langle \bar{k} \rangle_o$ are of relatively modest magnitude when compared with the linear ones. Increasing the pulsation amplitude might lead to more substantial contributions from nonlinear production terms and break down this scaling.
- (iv) For each case, profiles of oscillatory shear rate and resolved Reynolds stresses are characterized by oscillating waves which are advected away from the UCL at a constant speed while also being dissipated. Here ω is found to determine both the speeds of the oscillating waves and the extent of these waves, which identifies the Stokes layer thickness (δ_s). More specifically, δ_s was found to increase with decreasing ω , whereas the wave speed increased with ω . The scaling of δ_s has also been discussed, and findings have been used to propose a model for δ_s .

All in all, flow pulsation is found to have a significant impact on both longtime-averaged and phase-averaged flow statistics, with nuanced dependencies on oscillation amplitude and frequency. The observed enhancement of the longtime-averaged surface drag, the isotropization of turbulence in the UCL, and the presence of a Stokes layer, amongst others, are expected to have important implications on the exchange of mass, energy and momentum between the land surface and the atmosphere, as well as affect our ability to model these processes in weather forecasting and climate models. These models typically rely on surface flux parameterizations and theories that are based on flow stationarity assumptions and are not able to capture these behaviours correctly (see, e.g. Stensrud 2007). The proposed phenomenological models for z_0 and δ_s , as well as the identified scaling of phase- and intrinsic-averaged flow statistics, contribute to advancing our understanding of flow unsteadiness in the ABL and offer a pathway for the development of improved surface flux parameterizations. Given the massive parameter space of unsteady ABL flow processes, it is also essential to acknowledge that several questions remain unanswered and deserve further investigation. For example, what is the impact of different types of periodic and aperiodic flow unsteadiness on turbulence statistics and topology? How are these variations in the structure of turbulence impacting land–atmosphere exchange rates of momentum, energy and mass? Can prevailing surface flux parameterizations be modified to account for these impacts? Addressing these questions will be the subject of future studies.

Funding. This material is based upon work supported by, or in part by, the Army Research Laboratory and the Army Research Office under grant number W911NF-22-1-0178. This work used the Anvil supercomputer at Purdue University through allocation ATM180022 from the Advanced Cyberinfrastructure Coordination Ecosystem: Services & Support (ACCESS) program, which is supported by National Science Foundation grant nos. 2138259, 2138286, 2138307, 2137603 and 2138296. The authors acknowledge the Texas Advanced Computing Center (TACC) at The University of Texas at Austin for providing resources that have contributed to the research results reported within this paper.

Declaration of interests. The authors report no conflict of interest.

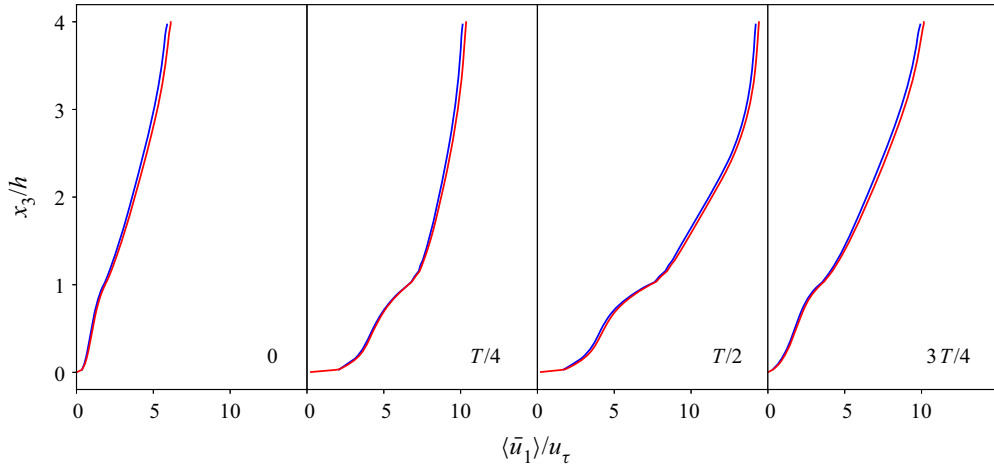


Figure 24. Phase- and intrinsic-averaged velocity $\langle \bar{u}_1 \rangle$ of LES400 (blue) and DNS400 figures (red).

Author ORCIDs.

 Marco G. Giometto <https://orcid.org/0000-0001-9661-0599>.

Appendix A. Wall-layer modelling considerations

As discussed in § 2, simulations have been conducted using an algebraic wall-layer model at the solid–fluid interface to evaluate tangential surface stresses. In this section, we show that the use of an equilibrium wall-layer model can be justified on the basis that the flow is in the fully rough aerodynamic regime.

An LES of flow over a single cube is carried out at roughness Reynolds number $Re_\tau = u_\tau h / \nu = 400$ (hereafter referred as to LES400), and results are compared with those from a DNS run (DNS400). At such a Reynolds number, the flow field is in fully rough regime, as also shown in Xie *et al.* (2008). The size of the computational domain is $[0, 3h] \times [0, 3h] \times [0, 4h]$, and the planar and frontal area densities are the same as those in the main simulations of the study. The forcing frequency and the oscillation amplitude are $\omega T_h = 0.125\pi$ and $\alpha = 0.8$, respectively, which are comparable to the ones considered in the study. The grid resolution of LES400 follows the main simulations, which is $(n_1, n_2, n_3) = (8, 8, 16)$ for each cube, and the identical wall-layer model as that in the main simulations is applied in the vicinity of the cube facets and the lower surface with the same roughness length scale. The grid resolution of DNS400 is $(n_1, n_2, n_3) = (64, 64, 128)$ per cube. Such a grid resolution ensures that the ratio between the grid size $\Delta = \sqrt[3]{\Delta_1 \Delta_2 \Delta_3}$ and the Kolmogorov scale η does not exceed 2, which has been proven sufficient for DNS of flow over fully rough surfaces (Zhang *et al.* 2022).

In both simulations, the contribution from the tangential stresses at the cube facets and lower surface to the total surface drag remains below 1 %, confirming that the flow is in the fully rough regime. Figures 24 and 25 display the phase- and intrinsic-averaged velocity ($\langle \bar{u}_1 \rangle$) and turbulent kinetic energy ($\langle \bar{k} \rangle$), respectively. Profiles from the LES400 case are in good agreement with corresponding DNS quantities, with the maximum error in the LES400 profiles relative to those from the DNS400 case being approximately 1 % and 6 % for $\langle \bar{u}_1 \rangle$ and $\langle \bar{k} \rangle$, respectively. The minor mismatches in $\langle \bar{k} \rangle$ can be partly explained by the fact that the SGS contribution to $\langle \bar{k} \rangle$ is zero for the LES400 case. It is suggested that, although the equilibrium assumption does not hold in a strict sense, the use of an

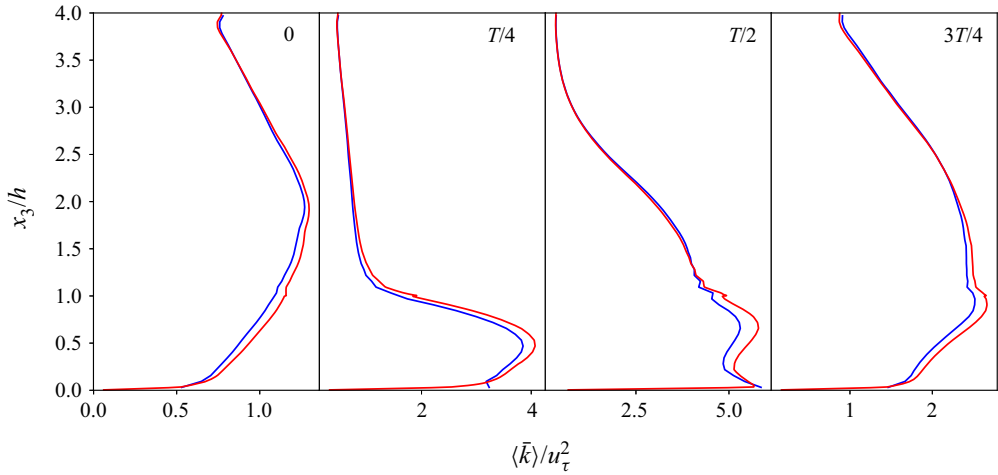


Figure 25. Phase- and intrinsic-averaged turbulent kinetic energy $\langle \bar{k} \rangle = (\langle \overline{u'_1 u'_1} \rangle + \langle \overline{u'_2 u'_2} \rangle + \langle \overline{u'_3 u'_3} \rangle) / 2$ of LES400 (blue) and DNS400 (red).

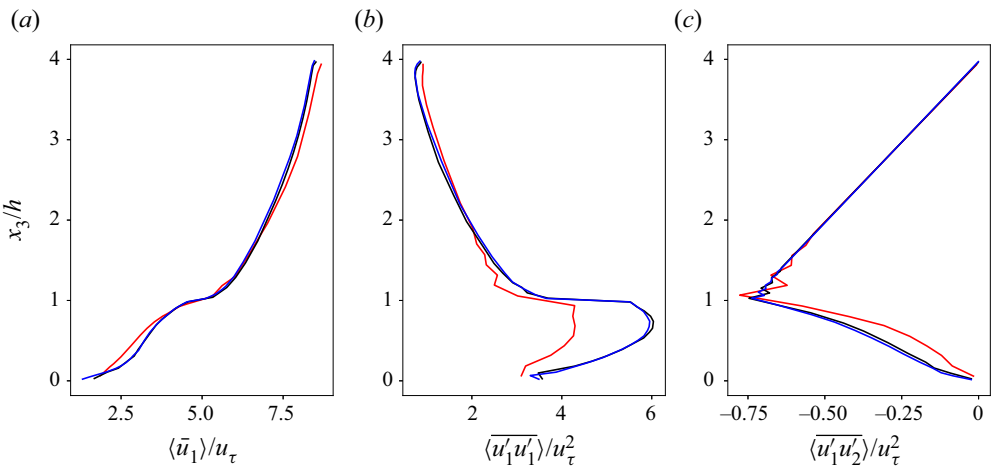


Figure 26. Comparison of the mean flow (a), resolved streamwise velocity variance (b), and resolved Reynolds shear stress (c) of the three test simulations for the resolution sensitivity analysis: red (4, 4, 8); black (8, 8, 16); blue (12, 12, 24).

equilibrium wall-layer model does not result in a noticeable impact on model results for the considered unsteady flow cases.

Appendix B. Resolution sensitivity analysis

To identify grid resolution requirements for simulations in this study, a grid-resolution sensitivity analysis has been conducted for the stationary flow case, i.e. $\alpha = 0$. The domain size for this analysis is $(36h, 12h, 4h)$, and we have studied the convergence of $\langle \bar{u}_1 \rangle$, $\langle \overline{u'_1 u'_1} \rangle$ and $\langle \overline{u'_1 u'_3} \rangle$ profiles as the grid stencil is progressively reduced. Three grid resolutions have been considered, namely (4, 4, 8), (8, 8, 16) and (12, 12, 24) on a per-cube basis. Note that the reduced domain size may have an impact on the evaluated flow statistics, but this

serves the purpose of this analysis, since we are here only interested in quantifying relative variations of selected profiles across grid resolutions. Other numerical and physical parameters of the grid-sensitivity analysis simulations are set equal to the ones used in the main simulations.

As apparent from figure 26, profiles from the (8, 8, 16) case are essentially matching corresponding ones from the (12, 12, 24) case, indicating that the chosen grid resolution for the pulsatile channel flow analysis is sufficient to yield grid-independent flow statistics (up to second order).

REFERENCES

- ALBERTSON, J.D. & PARLANGE, M.B. 1999a Natural integration of scalar fluxes from complex terrain. *Adv. Water Resour.* **23**, 239–252.
- ALBERTSON, J.D. & PARLANGE, M.B. 1999b Surface length scales and shear stress: implications for land-atmosphere interaction over complex terrain. *Water Resour. Res.* **35**, 2121–2132.
- ANDERSON, W. 2016 Amplitude modulation of streamwise velocity fluctuations in the roughness sublayer: evidence from large-eddy simulations. *J. Fluid Mech.* **789**, 567–588.
- ANDERSON, W., LI, Q. & BOU-ZEID, E. 2015 Numerical simulation of flow over urban-like topographies and evaluation of turbulence temporal attributes. *J. Turbul.* **16**, 809–831.
- AUVINEN, M., JÄRVI, L., HELLSTEN, A., RANNIK, Ü. & VESALA, T. 2017 Numerical framework for the computation of urban flux footprints employing large-eddy simulation and lagrangian stochastic modeling. *Geosci. Model Develop.* **10**, 4187–4205.
- BARLOW, J.F., HARMAN, I.N. & BELCHER, S.E. 2004 Scalar fluxes from urban street canyons. Part I. Laboratory simulation. *Boundary-Layer Meteorol.* **113**, 369–385.
- BASLEY, J., PERRET, L. & MATHIS, R. 2019 Structure of high Reynolds number boundary layers over cube canopies. *J. Fluid Mech.* **870**, 460–491.
- BENJAMIN, S.G., *et al.* 2016 A North American hourly assimilation and model forecast cycle: the rapid refresh. *Mon. Weath. Rev.* **144**, 1669–1694.
- BHAGANAGAR, K. 2008 Direct numerical simulation of unsteady flow in channel with rough walls. *Phys. Fluids* **20**, 101508.
- BÖHM, M., FINNIGAN, J.J., RAUPACH, M.R. & HUGHES, D. 2013 Turbulence structure within and above a canopy of bluff elements. *Boundary-Layer Meteorol.* **146**, 393–419.
- BOU-ZEID, E., MENEVEAU, C. & PARLANGE, M.B. 2004 Large-eddy simulation of neutral atmospheric boundary layer flow over heterogeneous surfaces: blending height and effective surface roughness. *Water Resour. Res.* **40**, W02505.
- BOU-ZEID, E., MENEVEAU, C. & PARLANGE, M.B. 2005 A scale-dependent lagrangian dynamic model for large eddy simulation of complex turbulent flows. *Phys. Fluids* **17**, 025105.
- BRERETON, G.J., REYNOLDS, W.C. & JAYARAMAN, R. 1990 Response of a turbulent boundary layer to sinusoidal free-stream unsteadiness. *J. Fluid Mech.* **221**, 131–159.
- BRITTER, R.E. & HANNA, S.R. 2003 Flow and dispersion in urban areas. *Annu. Rev. Fluid Mech.* **35**, 469–496.
- CANUTO, C., HUSSAINI, M.Y., QUARTERONI, A. & ZANG, T.A. 2007 *Spectral Methods: Evolution to Complex Geometries and Applications to Fluid Dynamics*. Springer Science & Business Media.
- CARR, I.A. & PLESNIAK, M.W. 2017 Surface obstacles in pulsatile flow. *Exp. Fluids* **58**, 1–11.
- CHAMECKI, M., MENEVEAU, C. & PARLANGE, M.B. 2009 Large eddy simulation of pollen transport in the atmospheric boundary layer. *J. Aerosol Sci.* **40**, 241–255.
- CHANG, Y.S. & SCOTTI, A. 2004 Modeling unsteady turbulent flows over ripples: Reynolds-averaged Navier–Stokes equations (RANS) versus large-eddy simulation (LES). *J. Geophys. Res. Oceans* **109**, C09012.
- CHAU, L. & BHAGANAGAR, K. 2012 Understanding turbulent flow over ripple-shaped random roughness in a channel. *Phys. Fluids* **24**, 115102.
- CHENG, H., HAYDEN, P., ROBINS, A.G. & CASTRO, I.P. 2007 Flow over cube arrays of different packing densities. *J. Wind Engng Ind. Aerodyn.* **95**, 715–740.
- CHENG, W. & PORTÉ-AGEL, F. 2015 Adjustment of turbulent boundary-layer flow to idealized urban surfaces: a large-eddy simulation study. *Boundary-Layer Meteorol.* **155**, 249–270.
- CHENG, W. & PORTÉ-AGEL, F. 2016 Large-eddy simulation of flow and scalar dispersion in rural-to-urban transition regions. *Intl J. Heat Fluid Flow* **60**, 47–60.

- CHESTER, S., MENEVEAU, C. & PARLANGE, M.B. 2007 Modeling turbulent flow over fractal trees with renormalized numerical simulation. *J. Comput. Phys.* **225**, 427–448.
- CHRISTEN, A., ROTACH, M.W. & VOGT, R. 2009 The budget of turbulent kinetic energy in the urban roughness sublayer. *Boundary-Layer Meteorol.* **131**, 193–222.
- CHRISTEN, A., VAN GORSEL, E. & VOGT, R. 2007 Coherent structures in urban roughness sublayer turbulence. *Intl J. Climatol.* **27**, 1955–1968.
- COCEAL, O. & BELCHER, S.E. 2004 A canopy model of mean winds through urban areas. *Q. J. R. Meteorol. Soc.* **130**, 1349–1372.
- COCEAL, O., DOBRE, A., THOMAS, T.G. & BELCHER, S.E. 2007 Structure of turbulent flow over regular arrays of cubical roughness. *J. Fluid Mech.* **589**, 375–409.
- EDWARDS, J.M., BEARE, R.J. & LAPWORTH, A.J. 2006 Simulation of the observed evening transition and nocturnal boundary layers: single-column modelling. *Q. J. R. Meteorol. Soc.* **132**, 61–80.
- ELSSINGA, G.E., POELMA, C., SCHRÖDER, A., GEISLER, R., SCARANO, F. & WESTERWEEEL, J. 2012 Tracking of vortices in a turbulent boundary layer. *J. Fluid Mech.* **697**, 273–295.
- FANG, J., DIEBOLD, M., HIGGINS, C. & PARLANGE, M.B. 2011 Towards oscillation-free implementation of the immersed boundary method with spectral-like methods. *J. Comput. Phys.* **230**, 8179–8191.
- FANG, J. & PORTÉ-AGEL, F. 2015 Large-eddy simulation of very-large-scale motions in the neutrally stratified atmospheric boundary layer. *Boundary-Layer Meteorol.* **155**, 397–416.
- FERNANDO, H.J.S. 2010 Fluid dynamics of urban atmospheres in complex terrain. *Annu. Rev. Fluid Mech.* **42**, 365–389.
- FREDSØE, J., ANDERSEN, K.H. & SUMER, B.M. 1999 Wave plus current over a ripple-covered bed. *Coast. Engng* **38**, 177–221.
- GIOMETTO, M.G., CHRISTEN, A., MENEVEAU, C., FANG, J., KRAFCZYK, M. & PARLANGE, M.B. 2016 Spatial characteristics of roughness sublayer mean flow and turbulence over a realistic urban surface. *Boundary-Layer Meteorol.* **160**, 425–452.
- GONÇALVES, R.T., FRANZINI, G.R., ROSETTI, G.F., MENEGHINI, J.R. & FUJARRA, A.L.C. 2015 Flow around circular cylinders with very low aspect ratio. *J. Fluids Struct.* **54**, 122–141.
- GRAHAM, J. & MENEVEAU, C. 2012 Modeling turbulent flow over fractal trees using renormalized numerical simulation: alternate formulations and numerical experiments. *Phys. Fluids* **24**, 125105.
- GRANT, W.D. & MADSEN, O.S. 1979 Combined wave and current interaction with a rough bottom. *J. Geophys. Res. Oceans* **84**, 1797–1808.
- GRANT, W.D. & MADSEN, O.S. 1986 The continental-shelf bottom boundary layer. *Annu. Rev. Fluid Mech.* **18**, 265–305.
- HICKS, B.B., PENDERGRASS, W.R., BAKER, B.D., SAYLOR, R.D., O'DELL, D.L., EASH, N.S. & MCQUEEN, J.T. 2018 On the relevance of $\ln(z_0/z_{0T}) = kb^{-1}$. *Boundary-Layer Meteorol.* **167**, 285–301.
- HOLTSLAG, A.A.M., *et al.* 2013 Stable atmospheric boundary layers and diurnal cycles: challenges for weather and climate models. *Bull. Am. Meteorol. Soc.* **94**, 1691–1706.
- HOOVER, J.D., STAUFFER, D.R., RICHARDSON, S.J., MAHRT, L., GAUDET, B.J. & SUAREZ, A. 2015 Submeso motions within the stable boundary layer and their relationships to local indicators and synoptic regime in moderately complex terrain. *J. Appl. Meteorol. Climatol.* **54**, 352–369.
- INAGAKI, A., CASTILLO, M.C.L., YAMASHITA, Y., KANDA, M. & TAKIMOTO, H. 2012 Large-eddy simulation of coherent flow structures within a cubical canopy. *Boundary-Layer Meteorol.* **142**, 207–222.
- KANDA, M., MORIWAKI, R. & KASAMATSU, F. 2004 Large-eddy simulation of turbulent organized structures within and above explicitly resolved cube arrays. *Boundary-Layer Meteorol.* **112**, 343–368.
- KASTNER-KLEIN, P. & ROTACH, M.W. 2004 Mean flow and turbulence characteristics in an urban roughness sublayer. *Boundary-Layer Meteorol.* **111**, 55–84.
- KATUL, G.G., MAHRT, L., POGGI, D. & SANZ, C. 2004 One-and two-equation models for canopy turbulence. *Boundary-Layer Meteorol.* **113**, 81–109.
- KEMP, P.H. & SIMONS, R.R. 1982 The interaction between waves and a turbulent current: waves propagating with the current. *J. Fluid Mech.* **116**, 227–250.
- KEULEGAN, G.H. & CARPENTER, L.H. 1958 Forces on cylinders and plates in an oscillating fluid. *J. Res. Natl Bur. Stand.* **60**, 423–440.
- KIM, J. & MOIN, P. 1985 Application of a fractional-step method to incompressible Navier–Stokes equations. *J. Comput. Phys.* **59**, 308–323.
- LETTAU, H. 1969 Note on aerodynamic roughness-parameter estimation on the basis of roughness-element description. *J. Appl. Meteorol.* **8**, 828–832.
- LI, D. & BOU-ZEID, E. 2011 Coherent structures and the dissimilarity of turbulent transport of momentum and scalars in the unstable atmospheric surface layer. *Boundary-Layer Meteorol.* **140**, 243–262.

Mean flow and turbulence in unsteady canopy layers

- LI, D. & BOU-ZEID, E. 2014 Quality and sensitivity of high-resolution numerical simulation of urban heat islands. *Environ. Res. Lett.* **9**, 055001.
- LI, Q. & BOU-ZEID, E. 2019 Contrasts between momentum and scalar transport over very rough surfaces. *J. Fluid Mech.* **880**, 32–58.
- LI, Q., BOU-ZEID, E., ANDERSON, W., GRIMMOND, S. & HULTMARK, M. 2016 Quality and reliability of LES of convective scalar transfer at high Reynolds numbers. *Intl J. Heat Mass Transfer* **102**, 959–970.
- LI, Q. & KATUL, G. 2022 Bridging the urban canopy sublayer to aerodynamic parameters of the atmospheric surface layer. *Boundary-Layer Meteorol.* **185**, 1–27.
- LOWE, R.J., KOSEFF, J.R. & MONISMITH, S.G. 2005 Oscillatory flow through submerged canopies: 1. Velocity structure. *J. Geophys. Res. Oceans* **110**, C10016.
- MACDONALD, R.W., GRIFFITHS, R.F. & HALL, D.J. 1998 An improved method for the estimation of surface roughness of obstacle arrays. *Atmos. Environ.* **32**, 1857–1864.
- MAHRT, L. 2007 The influence of nonstationarity on the turbulent flux–gradient relationship for stable stratification. *Boundary-Layer Meteorol.* **125**, 245–264.
- MAHRT, L. 2008 The influence of transient flow distortion on turbulence in stable weak-wind conditions. *Boundary-Layer Meteorol.* **127**, 1–16.
- MAHRT, L. 2009 Characteristics of submeso winds in the stable boundary layer. *Boundary-Layer Meteorol.* **130**, 1–14.
- MAHRT, L. & BOU-ZEID, E. 2020 Non-stationary boundary layers. *Boundary-Layer Meteorol.* **177**, 189–204.
- MAHRT, L., THOMAS, C., RICHARDSON, S., SEAMAN, N., STAUFFER, D. & ZEEMAN, M. 2013 Non-stationary generation of weak turbulence for very stable and weak-wind conditions. *Boundary-Layer Meteorol.* **147**, 179–199.
- MANNA, M., VACCA, A. & VERZICCO, R. 2012 Pulsating pipe flow with large-amplitude oscillations in the very high frequency regime. Part 1. Time-averaged analysis. *J. Fluid Mech.* **700**, 246–282.
- MANNA, M., VACCA, A. & VERZICCO, R. 2015 Pulsating pipe flow with large-amplitude oscillations in the very high frequency regime. Part 2. Phase-averaged analysis. *J. Fluid Mech.* **766**, 272–296.
- MAO, Z. & HANRATTY, T.J. 1986 Studies of the wall shear stress in a turbulent pulsating pipe flow. *J. Fluid Mech.* **170**, 545–564.
- MARGAIRAZ, F., GIOMETTO, M.G., PARLANGE, M.B. & CALAF, M. 2018 Comparison of dealiasing schemes in large-eddy simulation of neutrally stratified atmospheric flows. *Geosci. Model Develop.* **11**, 4069–4084.
- MARTINUZZI, R. & TROPEA, C. 1993 The flow around surface-mounted, prismatic obstacles placed in a fully developed channel flow. *Trans. ASME J. Fluids Engng* **115**, 85–92.
- MARUCCI, D. & CARPENTIERI, M. 2020 Stable and convective boundary-layer flows in an urban array. *J. Wind Engng Ind. Aerodyn.* **200**, 104140.
- MATHISEN, P.P. & MADSEN, O.S. 1996 Waves and currents over a fixed rippled bed: 2. Bottom and apparent roughness experienced by currents in the presence of waves. *J. Geophys. Res. Oceans* **101**, 16543–16550.
- MITTAL, R. & IACCARINO, G. 2005 Immersed boundary methods. *Annu. Rev. Fluid Mech.* **37**, 239–261.
- MOENG, C. 1984 A large-eddy-simulation model for the study of planetary boundary-layer turbulence. *J. Atmos. Sci.* **41**, 2052–2062.
- MOHD-YUSOF, J. 1996 *Interaction of Massive Particles with Turbulence*. Cornell University.
- MOMEN, M. & BOU-ZEID, E. 2017 Mean and turbulence dynamics in unsteady Ekman boundary layers. *J. Fluid Mech.* **816**, 209–242.
- MORISON, J.R., JOHNSON, J.W. & SCHAAF, S.A. 1950 The force exerted by surface waves on piles. *J. Petrol. Tech.* **2**, 149–154.
- MYRHAUG, D. & SLAATTELID, O.H. 1989 Combined wave and current boundary layer model for fixed rough seabeds. *Ocean Engng* **16**, 119–142.
- OMIDVAR, H., BOU-ZEID, E., LI, Q., MELLADO, J. & KLEIN, P. 2020 Plume or bubble? Mixed-convection flow regimes and city-scale circulations. *J. Fluid Mech.* **897**, A5.
- ÖNDER, A. & YUAN, J. 2019 Turbulent dynamics of sinusoidal oscillatory flow over a wavy bottom. *J. Fluid Mech.* **858**, 264–314.
- ORSZAG, S.A. 1970 Analytical theories of turbulence. *J. Fluid Mech.* **41**, 363–386.
- ORSZAG, S.A. & PAO, Y. 1975 Numerical computation of turbulent shear flows. *Adv. Geophys.* **18**, 225–236.
- PASCHEKE, F., BARLOW, J.F. & ROBINS, A. 2008 Wind-tunnel modelling of dispersion from a scalar area source in urban-like roughness. *Boundary-Layer Meteorol.* **126**, 103–124.
- PATEL, M.H. & WITZ, J.A. 2013 *Compliant Offshore Structures*. Butterworth-Heinemann.
- PATIL, A. & FRINGER, O. 2022 Drag enhancement by the addition of weak waves to a wave-current boundary layer over bumpy walls. *J. Fluid Mech.* **947**, A3.

- PATTENDEN, R.J., TURNOCK, S.R. & ZHANG, X. 2005 Measurements of the flow over a low-aspect-ratio cylinder mounted on a ground plane. *Exp. Fluids* **39**, 10–21.
- POGGI, D., KATUL, G.G. & ALBERTSON, J.D. 2004 Momentum transfer and turbulent kinetic energy budgets within a dense model canopy. *Boundary-Layer Meteorol.* **111**, 589–614.
- POPE, S.B. 2000 *Turbulent Flows*. Cambridge University Press.
- RAMAMURTHY, P., LI, D. & BOU-ZEID, E. 2017 High-resolution simulation of heatwave events in New York city. *Theor. Appl. Climatol.* **128**, 89–102.
- RAMAPRIAN, B.R. & TU, S. 1980 An experimental study of oscillatory pipe flow at transitional Reynolds numbers. *J. Fluid Mech.* **100**, 513–544.
- RAMAPRIAN, B.R. & TU, S.W. 1983 Fully developed periodic turbulent pipe flow. Part 2. The detailed structure of the flow. *J. Fluid Mech.* **137**, 59–81.
- RAUPACH, M.R. 1992 Drag and drag partition on rough surfaces. *Boundary-Layer Meteorol.* **60**, 375–395.
- RAUPACH, M.R., THOM, A.S. & EDWARDS, I. 1980 A wind-tunnel study of turbulent flow close to regularly arrayed rough surfaces. *Boundary-Layer Meteorol.* **18**, 373–397.
- REYNOLDS, R.T. & CASTRO, I.P. 2008 Measurements in an urban-type boundary layer. *Exp. Fluids* **45**, 141–156.
- ROTACH, M.W. 1993 Turbulence close to a rough urban surface part I: Reynolds stress. *Boundary-Layer Meteorol.* **65**, 1–28.
- ROTACH, M.W., *et al.* 2005 Bubble—an urban boundary layer meteorology project. *Theor. Appl. Climatol.* **81**, 231–261.
- ROTH, M. 2012 Urban heat islands. In *Handbook of Environmental Fluid Dynamics, Volume Two* (ed. H.J.S. Fernando), pp. 162–181. CRC Press.
- SADIQUE, J., YANG, X.I.A., MENEVEAU, C. & MITTAL, R. 2017 Aerodynamic properties of rough surfaces with high aspect-ratio roughness elements: effect of aspect ratio and arrangements. *Boundary-Layer Meteorol.* **163**, 203–224.
- SALESKY, S.T., CHAMECKI, M. & BOU-ZEID, E. 2017 On the nature of the transition between roll and cellular organization in the convective boundary layer. *Boundary-Layer Meteorol.* **163**, 41–68.
- SCHMID, M.F., LAWRENCE, G.A., PARLANGE, M.B. & GIOMETTO, M.G. 2019 Volume averaging for urban canopies. *Boundary-Layer Meteorol.* **173**, 349–372.
- SCOTTI, A. & PIOMELLI, U. 2001 Numerical simulation of pulsating turbulent channel flow. *Phys. Fluids* **13**, 1367–1384.
- SKAMAROCK, W.C., KLEMP, J.B., DUDHIA, J., GILL, D.O., BARKER, D.M., DUDA, M.G., HUANG, X.Y., WANG, W. & POWERS, J.G. 2008 A description of the advanced research WRF version. *NCAR Tech. Rep.* TN-556+STR.
- SLEATH, J.F. 1991 Velocities and shear stresses in wave-current flows. *J. Geophys. Res. Oceans* **96**, 15237–15244.
- SOULSBY, R.L., HAMM, L., KLOPMAN, G., MYRHAUG, D., SIMONS, R.R. & THOMAS, G.P. 1993 Wave-current interaction within and outside the bottom boundary layer. *Coast. Engng* **21**, 41–69.
- STANISLAS, M., PERRET, L. & FOUCAUT, J. 2008 Vortical structures in the turbulent boundary layer: a possible route to a universal representation. *J. Fluid Mech.* **602**, 327–382.
- STENSRUD, D.J. 2007 *Parameterization Schemes*. Cambridge University Press.
- STOKES, G.G. 1901 On the effect of the internal friction of fluids on the motion of pendulums. *Trans. Camb. Phil. Soc.* **9**, 1–141.
- STULL, R.B. 1988 *An Introduction to Boundary Layer Meteorology*, vol. 13. Springer Science & Business Media.
- TARDU, S.F. 2005 Spectral characteristics of the near-wall turbulence in an unsteady channel flow. *J. Appl. Mech.* **74**, 172–175.
- TARDU, S.F. & BINDER, G. 1993 Wall shear stress modulation in unsteady turbulent channel flow with high imposed frequencies. *Phys. Fluids A* **5**, 2028–2037.
- TARDU, S.F., BINDER, G. & BLACKWELDER, R.F. 1994 Turbulent channel flow with large-amplitude velocity oscillations. *J. Fluid Mech.* **267**, 109–151.
- TOMAS, J.M., POURQUIE, M. & JONKER, H. 2016 Stable stratification effects on flow and pollutant dispersion in boundary layers entering a generic urban environment. *Boundary-Layer Meteorol.* **159**, 221–239.
- TU, S.W. & RAMAPRIAN, B.R. 1983 Fully developed periodic turbulent pipe flow. Part 1. Main experimental results and comparison with predictions. *J. Fluid Mech.* **137**, 31–58.
- WENG, C., BOIJ, S. & HANIFI, A. 2016 Numerical and theoretical investigation of pulsatile turbulent channel flows. *J. Fluid Mech.* **792**, 98–133.

Mean flow and turbulence in unsteady canopy layers

- XIE, Z. & CASTRO, I.P. 2006 LES and RANS for turbulent flow over arrays of wall-mounted obstacles. *Flow Turbul. Combust.* **76**, 291–312.
- XIE, Z., COCEAL, O. & CASTRO, I.P. 2008 Large-eddy simulation of flows over random urban-like obstacles. *Boundary-Layer Meteorol.* **129**, 1–23.
- YANG, J. & ANDERSON, W. 2018 Numerical study of turbulent channel flow over surfaces with variable spanwise heterogeneities: topographically-driven secondary flows affect outer-layer similarity of turbulent length scales. *Flow Turbul. Combust.* **100**, 1–17.
- YANG, S., TAN, S., LIM, S. & ZHANG, S. 2006 Velocity distribution in combined wave–current flows. *Adv. Water Resour.* **29**, 1196–1208.
- YANG, X.I.A. 2016 On the mean flow behaviour in the presence of regional-scale surface roughness heterogeneity. *Boundary-Layer Meteorol.* **161**, 127–143.
- YANG, X.I.A. & MENEVEAU, C. 2016 Recycling inflow method for simulations of spatially evolving turbulent boundary layers over rough surfaces. *J. Turbul.* **17**, 75–93.
- YANG, X.I.A., SADIQUE, J., MITTAL, R. & MENEVEAU, C. 2016 Exponential roughness layer and analytical model for turbulent boundary layer flow over rectangular-prism roughness elements. *J. Fluid Mech.* **789**, 127–165.
- YU, X., ROSMAN, J.H. & HENCH, J.L. 2018 Interaction of waves with idealized high-relief bottom roughness. *J. Geophys. Res. Oceans* **123**, 3038–3059.
- YU, X., ROSMAN, J.H. & HENCH, J.L. 2022 Boundary layer dynamics and bottom friction in combined wave–current flows over large roughness elements. *J. Fluid Mech.* **931**, A11.
- YUAN, J. & MADSEN, O.S. 2015 Experimental and theoretical study of wave–current turbulent boundary layers. *J. Fluid Mech.* **765**, 480–523.
- ZHANG, W., ZHU, X., YANG, X.I.A. & WAN, M. 2022 Evidence for Raupach *et al.*'s mixing-layer analogy in deep homogeneous urban-canopy flows. *J. Fluid Mech.* **944**, A46.
- ZHU, X., IUNGO, G.V., LEONARDI, S. & ANDERSON, W. 2017 Parametric study of urban-like topographic statistical moments relevant to a priori modelling of bulk aerodynamic parameters. *Boundary-Layer Meteorol.* **162**, 231–253.